

Research paper

# Ball-milling treatment of gas-atomized Ti—48Al—2Cr—2Nb powder and its effect on preventing smoking during electron beam powder bed fusion building process

Seungkyun Yim<sup>a</sup>, Huakang Bian<sup>b,\*</sup>, Kenta Aoyagi<sup>b,\*</sup>, Keiji Yanagihara<sup>b</sup>, Shin-ichi Kitamura<sup>c</sup>, Hironobu Manabe<sup>c</sup>, Yohei Daino<sup>d</sup>, Yuichiro Hayasaka<sup>e</sup>, Kenta Yamanaka<sup>b</sup>, Akihiko Chiba<sup>b,\*</sup>

<sup>a</sup> Department of Materials Processing, Tohoku University, 6-6-02 Aobayama, Sendai, Miyagi 980-8579, Japan

<sup>b</sup> Institute for Materials Research, Tohoku University, 2-1-1 Katahira, Sendai, Miyagi 980-8577, Japan

<sup>c</sup> Advanced & Fundamental Technology Center Assistant General Manager, JEOL Ltd., Akishima, Tokyo 196-8558, Japan

<sup>d</sup> 3D Additive Manufacturing Project Development Group, JEOL Ltd., Akishima, Tokyo 196-8558, Japan

<sup>e</sup> The Electron Microscopy Center, Tohoku University, 2-1-1 Katahira, Aobaku, Sendai 980-8577, Japan

## ARTICLE INFO

### Keywords:

Electron beam powder bed fusion

Oxide film

Powder bed smoke

Mechanical ball milling

Titanium-aluminide alloy

## ABSTRACT

Smoking is the explosive powder-scattering by Coulomb interaction, and it is a difficult issue to avoid in electron beam powder bed fusion (EB-PBF) process. In this study, we investigated the effectiveness of mechanical ball milling to prevent powder-bed smoking in EB-PBF using gas-atomized Ti—48Al—2Cr—2Nb powder. The surface of the gas-atomized powder was confirmed to be composed of outer porous TiO<sub>2</sub> + Al<sub>2</sub>O<sub>3</sub> and inner dense Al<sub>2</sub>O<sub>3</sub> rich bilayer oxide film that gives rise to a high electrical resistance. The electrical resistivity after ball milling with 300 rpm (BM300) was significantly decreased due to the formation of the degenerated TiO<sub>2</sub> and Ti<sub>n</sub>O<sub>2n-1</sub>-type suboxide. The electrical equivalent circuit of the powder bed of BM300 was essentially a single resistor-capacitor (RC) circuit, owing to the mechanically deformed outer oxide film. Besides, through ball milling at 300 rpm for 30 min, the relaxation time of the gas-atomized powder was significantly decreased 1/16 times, and its electrostatic force decreased approximately 1/57 times. Finally, the suppressing effect of smoking on the EB-PBF building process was experimentally examined using ball-milled powders. It was clearly demonstrated that mechanical ball milling is an effective method to restrict smoking during the EB-PBF building process without any chemical treatment and composition change.

## 1. Introduction

Lightweight  $\gamma$ -TiAl alloys possess outstanding properties, such as high melting point, low density, high stiffness, and intrinsic strength retention. Therefore, Ni-based superalloys can be partially substituted by  $\gamma$ -TiAl alloys at operating temperatures ranging from 600 to 900 °C [1]. The main limitation pertaining to the industrial applications of  $\gamma$ -TiAl alloys is that the fabrication process is difficult using conventional techniques, such as casting, thermomechanical treatment, and hot deformation, owing to the inherent low ductility and brittle cracking of intermetallic compounds [2]. In recent years, additive manufacturing (AM) techniques have demonstrated the competitive advantages of fabricating metal parts with a complex design based on computer-aided design [3]. Dense  $\gamma$ -TiAl parts have been manufactured through electron

beam powder bed fusion manufacturing (EB-PBF), a type of AM, performed at a high preheating temperature (above 1100 °C), to suppress their high crack susceptibility [4,5]. Nevertheless, one of the problems in applying EB-PBF for manufacturing  $\gamma$ -TiAl parts is the explosive powder-scattering by Coulomb interaction during the EB-PBF building process, also known as “smoking” [6]. Until now, restricting methods for smoking events have mainly been developed through trial-and-error optimization, focusing on machinery control. The rule of thumb to restrict smoking is related to the following factors: using a defocused electron beam, adapting large powder, keying of the building plate, optimization of process parameters (i.e. beam current, scan speed, scan patterns), and using higher preheating temperature [7–10]. There are a couple of new approaches using a biased substrate that could be mentioned, although the academic literature on this is very sparse.

\* Corresponding authors.

E-mail addresses: [huakang.bian.d5@tohoku.ac.jp](mailto:huakang.bian.d5@tohoku.ac.jp) (H. Bian), [kenta.aoyagi.e7@tohoku.ac.jp](mailto:kenta.aoyagi.e7@tohoku.ac.jp) (K. Aoyagi), [akihiko.chiba.d3@tohoku.ac.jp](mailto:akihiko.chiba.d3@tohoku.ac.jp) (A. Chiba).

<https://doi.org/10.1016/j.addma.2022.102634>

Received 9 September 2021; Received in revised form 28 December 2021; Accepted 17 January 2022

Available online 20 January 2022

2214-8604/© 2022 Published by Elsevier B.V.

However, these methods are empirical and depend on uncertain factors and are not consistently effective.

One key factor causing smoking is the surface state of the metal powder that is encapsulated by an electrically insulating oxide film [10]. This oxide layer can act as a capacitor to inhibit charge redistribution across the particle contacts [9,10]. During the EB-PBF building process, the metal powder bed is preheated and selectively melted to solidify them into designed bulk parts in a layer-by-layer manner using a high-voltage electron beam. If the irradiated electrons are accumulated in the powder bed, the negatively charged particles mutually repel each other and explosively scatter into a vacuum chamber by Coulomb interaction [11]. During the building process, smoking must be avoided because the scattered powder clouds can remove the powder feedstock and prevent electron beam penetration, resulting in a build failure. Sigl et al. [7] has demonstrated that the electrostatic overcharge of powder particles is the major factor causing smoking in the powder bed. Eschey et al. [8] has suggested that the charge of the powder bed depends on the electrical resistance between the particles, owing to their extremely small contact areas. Cordero et al. [9] reported that powder-bed charging is predominantly affected by the relaxation times associated with their surface states, based on the developed analytical model. Therefore, it is essential to manipulate the powder surface to avoid smoking of the powder bed during the EB-PBF building process. However, the research on surface treatments to prevent smoking in the EB-PBF building process is inadequate.

Recently, our research group reported that the electrical resistivity of Inconel 718 powder was greatly reduced by mechanical stimulation, and smoking did not occur after ball milling, even when the powder bed was not preheated [10]. According to Mott [12], the oxide of a 3d transition metal whose d band is not completely filled is an insulator, but it has been found that the transition to metal is caused by the introduction of lattice strain [13]. Their studies are the first to find that the electrical properties of the Inconel 718 powder, which is covered with a thin oxide film of 3d transition metal can be transitioned from an insulator to metal by mechanical stimulation using a ball milling [10]. On the other hand, the surface oxide film of TiAl powder could also be covered with Ti oxide, which is a 3d transition metal, and could undergo metal-insulator transition by ball milling. Therefore, in this study, the mechanical ball milling was conducted to modify the powder surface to avoid smoking during the EB-PBF building process. The gas-atomized Ti–48Al–2Cr–2Nb powder was selected to investigate the influence of ball milling on the powder surface at various rotation speeds. The electrical equivalent circuit (EEC) of the powder bed in the EB-PBF building process was investigated based on impedance spectroscopy, and a quantitative factor was established to estimate the electrostatic force through electrical charging of the powder bed. Finally, the suppressing effect of smoking in the EB-PBF building process was experimentally validated using ball-milled powders.

## 2. Materials and methods

### 2.1. Mechanical ball milling

Commercial gas-atomized Ti–48Al–2Cr–2Nb powder was sourced from Daido Steel Co., Ltd. The chemical composition was examined via inductively coupled plasma mass spectrometry (ARCOS ICP-OES, SPECTRO Analytical Instruments, Germany), as shown in Table 1. To modify the powder surface, the gas-atomized Ti–48Al–2Cr–2Nb powder was mechanically ball-milled using a planetary high-energy ball milling machine (Pulverisette 7, Fritsch GmbH, Germany) for 30 min in

**Table 1**  
Alloying composition of gas-atomized Ti–48Al–2Cr–2Nb determined via ICP.

Element	Ti	Al	Cr	Nb	O
at%	46.18	49.58	1.85	2.24	0.14

an air atmosphere. The large disk and vial rotated in opposite directions, and the ranges of rotation speeds were 200, 250, 300, 350, and 400 rpm, with an interval of 50 rpm, and the respective powders were referred to as BM200, BM250, BM300, BM350, and BM400, respectively. Powder and tungsten carbide (WC) balls (with a diameter of 6 mm) were placed in a stainless-steel vial with a volume ratio of 33.3%.

### 2.2. Powder characterization

The particle size distribution of the powders was investigated using a laser particle size analyzer (LS 230, Beckman Coulter, Inc., USA). The oxygen content of all the powders was measured via inert gas fusion using an oxygen-nitrogen analyzer (ON736, Leco Corp., Japan). The crystal structures of the powders were observed via X-ray diffraction (XRD) using a Cu K $\alpha$  source at 45 kV and 40 mA (Philips X'PERT MPD, Malvern Panalytical, United Kingdom). Quantitative phase analysis using the Rietveld method was performed using the MAUD software. The morphologies of the raw and ball-milled powders were observed via scanning electron microscopy (SEM, S-3400 N, Hitachi High-Tech Science Corp., Japan). The surface contamination of ball-milled powders was analyzed via energy dispersive spectroscopy analysis using the benchtop SEM (JCM-6000, JEOL Ltd., Japan). Even under the high milling velocity > 350 rpm, the W and C elements were below 0.71 and 0.13 wt% on the surface of ball-milled powders, which is comparable to that of raw powder (0.63 and 0.14 wt%), respectively. Therefore, the effect of W and C elements on the electrical properties of ball-milled powders was neglected. Scanning/transmission electron microscopy analysis (STEM, Titan<sup>3</sup>™ 60–300 with double Cs-corrector, FEI-Company) was performed to further detail the morphology and composition of the powder surface. The samples for TEM investigation were prepared using a focused ion beam workstation (FIB, Helios Nano-lab 600i, FEI, USA). The powder surface was coated with platinum and carbon to protect its surface structure from an irradiated ion beam.

### 2.3. X-ray photoelectron spectroscopy (XPS) analysis

The surface chemical composition of the raw and ball-milled powders was determined via XPS (PHI5000 VersaProbe II, ULVAC-PHI Inc., Japan) using a monochromatic Al K $\alpha$  source (1486.7 eV). The powder samples were distributed on the carbon tape and then compressed using hand press. The survey spectra were collected to identify major chemical elements as following: O 1s, Ti 2p, Al 2p, Cr 2p, and Nb 3d. The high-resolution narrow-scan profiles were conducted to determine further detail of surface chemical composition. The XPS spectra were analyzed using Common Data Processing System (Version 12) with the Shirley background. The peak position was calibrated using the detected strong C 1s peak (284.8 eV) that most probably introduced during sample preparation [14]. XPS depth profiling was performed to estimate the oxide film thickness using the Ar<sup>+</sup> ion gun with a kinetic energy of 1 keV, providing an etching rate of 13.6 nm/min, as calibrated based on the SiO<sub>2</sub> standard.

### 2.4. Direct current resistivity and impedance spectroscopy test

To evaluate the direct current (DC) electrical resistivity of the powders, a four-point probe measurement was performed using a tailored contact device that enabled functioning based on powders in a vacuum environment (< 4.5 × 10<sup>-4</sup> Pa). A powder sample (2.45 g) was placed inside a measuring Al<sub>2</sub>O<sub>3</sub> cylinder, and both sides were sealed by circular nickel electrodes with a diameter of 10 mm. After that, the upper electrode was compressed by the load punch with the compressive force of 7 N to ensure a constant contact area under the vacuum environment. The temperature-dependent DC electrical resistivity was measured at a heating rate of 5 °C/min up to 800 °C. After that, the powder was held at 800 °C for 1 h and then furnace-cooled to room temperature. The impedance spectroscopy measurement was performed to characterize

further detail of electrical properties, such as resistance, capacitance, inductance. The electrical parameters were controlled and recorded by a multichannel AD converter, and the impedance was measured in the frequency range of 1 Hz to  $2 \times 10^6$  Hz using an LCR meter (ZM 2376 LCR, NF Corp., Japan). The measured impedance data was approximated using the software package EC-LAB (BioLogic Science Instruments Ltd., France) with the possible EEC models.

### 2.5. Smoking experiment in EB-PBF process

The powder bed smoke experiment during preheating in the EB-PBF building process was performed using a JEOL EB-PBF machine (JBS-Z0100EBM, JEOL Ltd., Japan). The powder was placed in a machined square hole ( $10 \times 10 \times 1 \text{ mm}^3$ ) at the center of the stainless-steel base plate ( $100 \times 100 \times 10 \text{ mm}^3$ ). After that, powder spreading was conducted to eliminate overflow powder from the base plate. Preheating was conducted under the conditions of accelerating voltage of 60 kV, a beam current of 5 mA, a scanning speed of 200 m/s, and the scanning pattern was a snake shape at room temperature (approximately 25 °C) under the vacuum environment ( $< 10^{-3}$  Pa). The occurrence of smoking was determined using recorded high-speed camera images with a 250 frame per second.

## 3. Results

### 3.1. Gas-atomized and ball-milled Ti–48Al–2Cr–2Nb powder

Fig. 1a shows the morphology of the gas-atomized Ti–48Al–2Cr–2Nb powder, most of which possessed a spherical shape. The average particle size was 71.71  $\mu\text{m}$ , with a broad size

distribution (Fig. 1c). The cross-sectional microstructure (Fig. 1b) observed from the backscattered electron (BSE) and X-ray profiles (Fig. 1d) suggests  $\gamma$ -TiAl and  $\alpha_2$ -Ti<sub>3</sub>Al phases with dendritic structures in the gas-atomized Ti–48Al–2Cr–2Nb powders.

The surface morphologies of the raw and ball-milled powders under various ball-milling conditions are shown in Fig. 2a–f. An irregular flexural surface was observed in the raw powder, owing to the high cooling rate during the gas atomization process [15]. The partially deformed surface (relatively smooth) on the BM200 powder was confirmed, as indicated by the red circle in Fig. 2b. The smooth area increased in the BM250 powder, as indicated by the red circle in Fig. 2c. In the BM300 and BM350 powders, almost the entire surface became smooth (Fig. 2d and e). The powder deformation became more severe with the increasing milling velocities above 350 rpm, causing non-spherical powders, as indicated by the yellow arrow in Fig. 2e and f.

The measured particle sizes of the raw and ball-milled powders under various ball-milling conditions are plotted in Fig. 3. The average particle size gradually decreased after ball milling to that of BM300; it nonetheless increased from that of BM300 to that of BM400. The  $d_{90}$  of the ball-milled powders gradually increased up to BM300, and thereafter rapidly increased from BM350, owing to the formation of large agglomerates (approximately 200  $\mu\text{m}$ ). This suggests that the pulverization related to the formation of a fresh surface is the dominant milling process for rotation speeds below 300 rpm, while agglomeration is the predominant milling process for milling velocities above 350 rpm, owing to the supplied high impact energy [16]. The calculated impact force and maximum deformation depth by the collision between the WC ball and Ti–48Al–2Cr–2Nb particle depending on milling velocities can be found in appendix 1.

The X-ray profiles of the raw and ball-milled powders are shown in

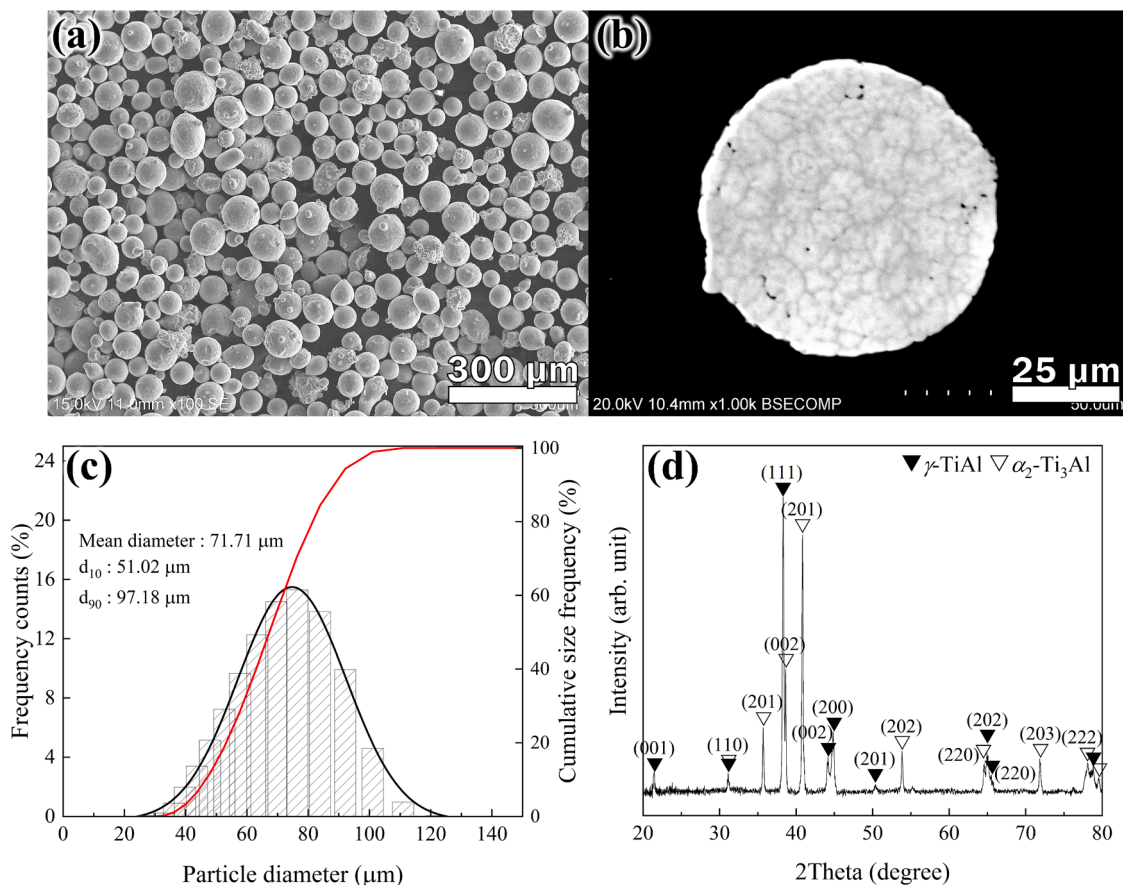
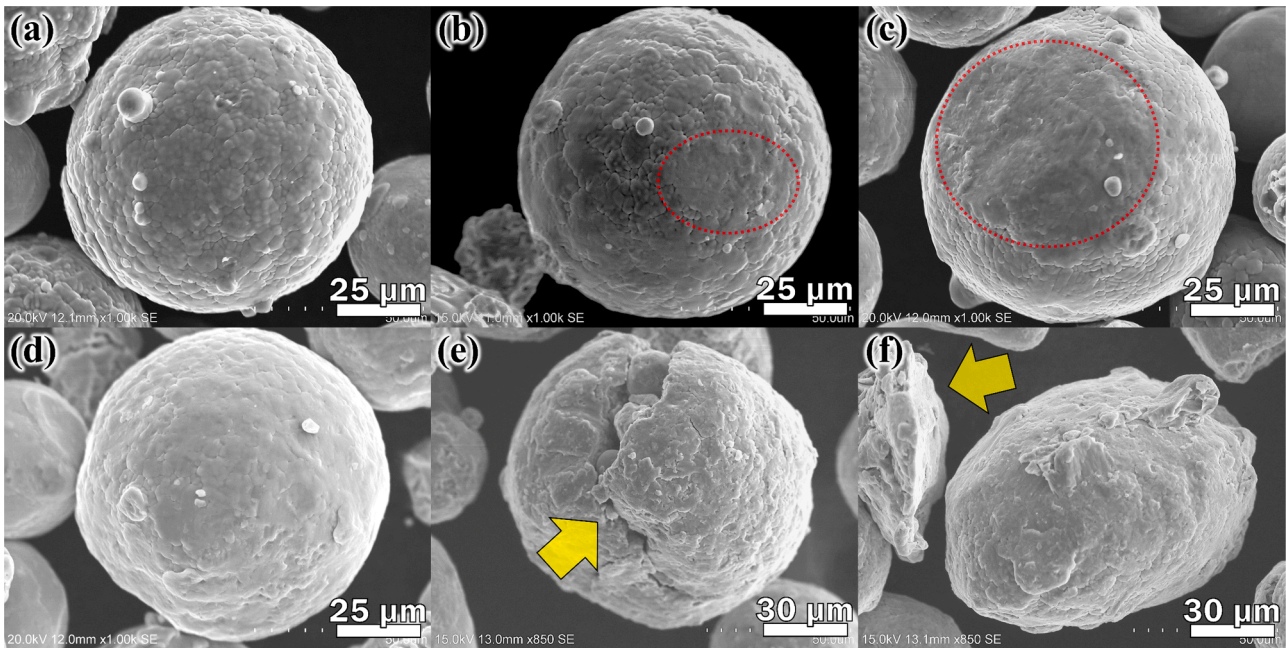
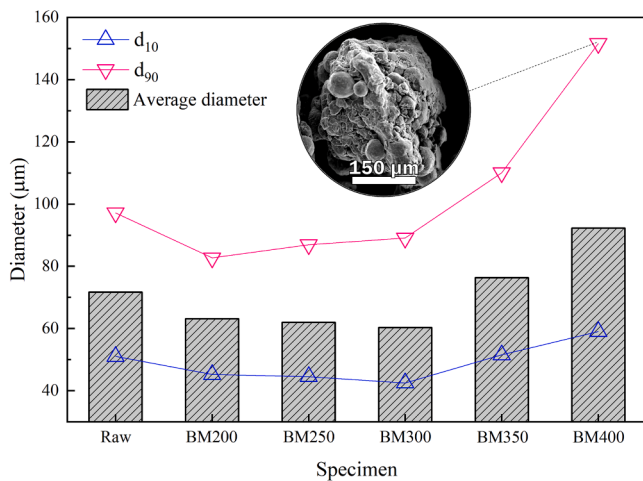


Fig. 1. Microstructure and particle size of gas-atomized Ti–48Al–2Cr–2Nb; (a) SEM image of surface, (b) BSE image of cross-section, (c) particle size distribution, and (d) XRD result.



**Fig. 2.** Surface morphology of Ti–48Al–2Cr–2Nb powders; (a) gas-atomized, (b) BM200, (c) BM250, (d) BM300, (e) BM350, (f) BM400. (Red circle indicates partially deformed region, yellow arrows indicate fractured particles). (For interpretation of the references to colour in this figure, the reader is referred to the web version of this article.)



**Fig. 3.** Size distribution of gas-atomized and ball-milled Ti–48Al–2Cr–2Nb powders under various milling velocities and corresponding BSE image.

Fig. 4, and all the profiles consist of  $\gamma$ -TiAl and  $\alpha_2$ -Ti<sub>3</sub>Al peaks, while the peaks broadened after ball milling. Quantitative phase analysis was performed using the Rietveld method to determine the relative weight fraction of each phase. The phase fraction of  $\alpha_2$ -Ti<sub>3</sub>Al increased up to that in case of BM300 and thereafter decreased above that for BM350, as shown in Fig. 4. The oxygen content of the raw powder gradually increased with increasing milling velocities up to 300 rpm, while it was maintained above 350 rpm, as shown in Table 2. Oxygen is known to be a strong  $\alpha_2$  phase stabilizer in  $\gamma$ -TiAl alloys [17]. Therefore, the increased  $\alpha_2$  fraction after ball milling could be due to the oxygen contamination from the air atmosphere. This result suggests that the oxide film thickness in ball-milled powder could be increased at milling velocity above 300 rpm by consuming solute oxygen with the  $\alpha_2 \rightarrow \gamma$  reaction.

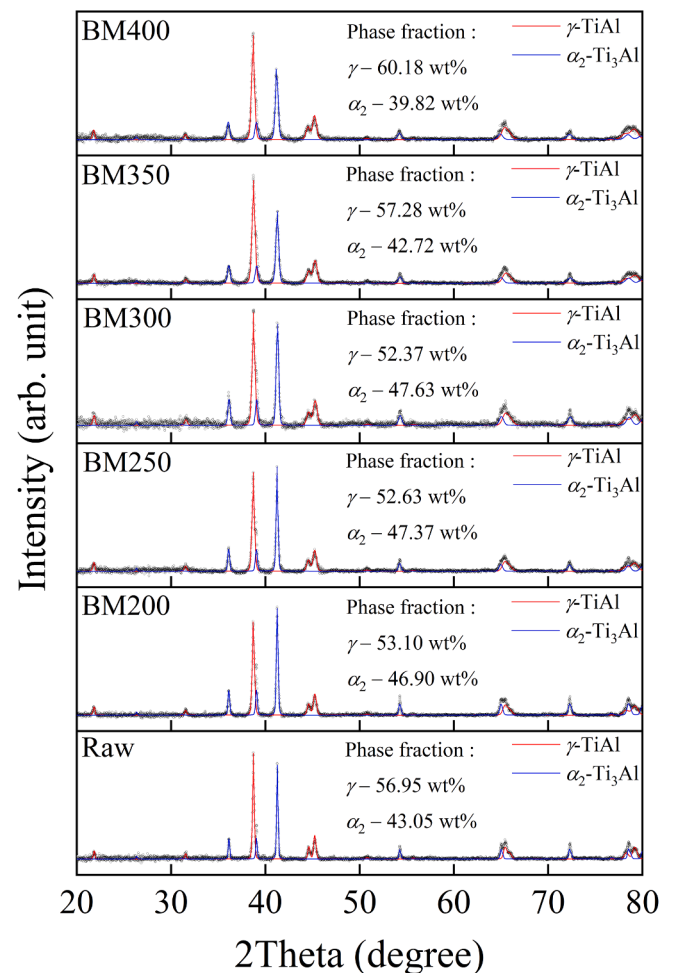


**Fig. 4.** XRD results of raw and ball-milled Ti–48Al–2Cr–2Nb powders depending on the milling velocities.

**Table 2**  
Oxygen concentration of raw and ball-milled powders.

Specimen	Raw	BM200	BM250	BM300	BM350	BM400
O concentration (wt%)	0.0632	0.0755	0.0867	0.1125	0.1100	0.1115

### 3.2. Electrical properties of powders

#### 3.2.1. Direct current electrical resistivity

The DC electrical resistivity of raw and ball-milled powders at room temperature is presented in Fig. 5a. The electrical resistivity of the raw powder was high and comparable to those of insulating or dielectric materials. This could be attributed to indirect contact between neighboring metal particles through the surface oxide films. The resistivity of raw powder was gradually decreased, and it was decreased to approximately 1/6 times in BM300 powder. For the BM350 and BM400 powders, the resistivity dropped by approximately  $10^{-7}$  magnitude compared to the raw powder. The temperature-dependent DC electrical resistivity of the raw and BM400 is presented in Fig. 5b. Upon heating, the electrical resistivity of the raw powder decreased, converging to the order of  $2.17 \times 10^{-4} \Omega\cdot\text{m}$ , which is similar to a metallic conductor, while that of BM400 powder was slightly decreased above  $400^\circ\text{C}$  to approximately  $1.87 \times 10^{-4} \Omega\cdot\text{m}$ . During the heating at  $800^\circ\text{C}$  for 1 h, the resistivity of raw and BM400 powders was preserved, and both powders were very loosely sintered after cooling. Thus, the rapid drop in electrical resistivity of the raw powder during heating predominantly originated from the properties of the surface oxide film, rather than the sintering between the particles. It is well known that the oxide of 3d transition metal suffers the metal-insulator transition at a high temperature [12,18]. The room temperature resistivity of BM350 and BM400 is reminiscent of the metal-insulator transition of Mott insulators. From these experimental results, it can be concluded that ball milling can increase the electrical conductivity of the surface oxide film that contained 3d transition metal oxide. The ball milling effect on electrical properties is further discussed in Section 4.2.

#### 3.2.2. Impedance spectroscopy analysis

A schematic of the EB-PBF building process with the corresponding EEC can be shown in Fig. 6a and c according to the previous study [10]. In the EEC model for the EB-PBF building process,  $I_{EB}$  is the amount of irradiated electron beam current,  $R_{PB}$  and  $C_{PB}$  are parallel resistors and capacitors of the powder bed, respectively,  $R_{BP}$  is the resistor of the base plate, and  $I_G$  is the discharged current through the ground wire. An extremely small contact area between the spherical particles can result in a high electrical resistance [19]. Moreover, a capacitor is formed when two conducting components are isolated using a nonconducting material. Therefore, the electrical charging of the powder bed is predominantly affected by the RC circuit during the EB-PBF building

process [7–10] as indicated by the red box in Fig. 6c. To evaluate the RC circuit of the raw and ball-milled powders, an impedance spectroscopy test was conducted, as shown in Fig. 6b and d. In the impedance test, each particle of the placed powder was assumed to be in a connected state, and the current was transferred through the connected network consisted of conductive metal and oxide film [19]. Therefore, the EEC of the powder bed is predominantly affected by their oxide film states. A typical example of the Nyquist plot with single RC circuit of a powder is shown in Fig. 6d. In the Nyquist plot, the x-intercept of the semicircular arc represents the metallic core resistance ( $R_m$ ) and oxide film resistance ( $R_{oxide}$ ) in the high-frequency and low-frequency ranges, respectively.

The Nyquist plots of the imaginary versus the real impedance components with respect to the frequency variations of the raw and ball-milled powders are presented in Fig. 7a and b. A semicircular arc shape wherein the center was slightly depressed along the x-axis was observed in all the powder specimens. On one hand, for all the powders, there was no significant difference observed in the  $R_m$  value, regardless of ball milling, while the diameter of the semicircle ( $R_{oxide}$ ) decreased with the increasing milling velocities up to 300 rpm (Fig. 7a). On the other hand, the imaginary component of the impedance in the BM350 and BM400 powders changed to a positive value associated with the inductive response in the high-frequency range (Fig. 7b).

The relationship between the phase angles and frequency, determining the number of time constants, is presented in the Bode plots (Fig. 8a–f). The real impedance in the raw powder was maintained in the low-frequency range, and the phase angle was below  $-5^\circ$ , indicating a dominant contribution of the resistor [20]. In the intermediate frequency range, the  $-45^\circ$  slope in  $\log Z'$  versus  $\log f$  frequency was observed to be related to the characteristics of the passive oxide film [21]. The multiple phase angle peaks were identified in the high-frequency range of  $-67^\circ$  to  $-78^\circ$  in the raw, BM200, and BM250 powders. This indicates that its electrical circuit would contain at least two time constants. The single-phase angle peak at  $-77^\circ$  was detected in BM300, representing a single time constant. In contrast, the phase angles of the BM350 and BM400 powders were changed to positive values of  $65^\circ$  and  $62^\circ$ , respectively.

The impedance spectra of each powder were quantitatively evaluated using the EEC model fitting. The two types (Type 1 and 2) of the EEC model that has already been used for fitting Ti and TiAl alloys in electrochemical impedance spectroscopy (EIS) tests [22,23], are displayed in Fig. 9a and b. Type 3 of the EEC model was suggested to explain the inductive reactance behavior in BM350 and BM400 powders [24]. The constant phase element (CPE) is used to explain the non-ideal behavior of the capacitances as follows:

$$Z_{CPE} = [Q(i\omega)^n]^{-1}, \quad (1)$$

where  $Q$  is the CPE constant of the passive oxide film,  $i$  is the imaginary number ( $i^2 = -1$ ), and  $n$  is the CPE exponent that is related to the

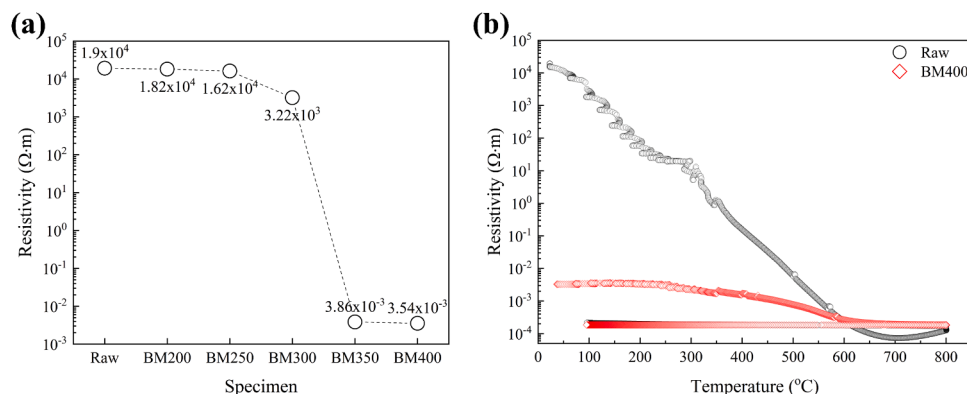


**Fig. 5.** Direct current electrical resistivity of raw and ball-milled Ti–48Al–2Cr–2Nb powders; (a) room temperature, (b) temperature-dependent.

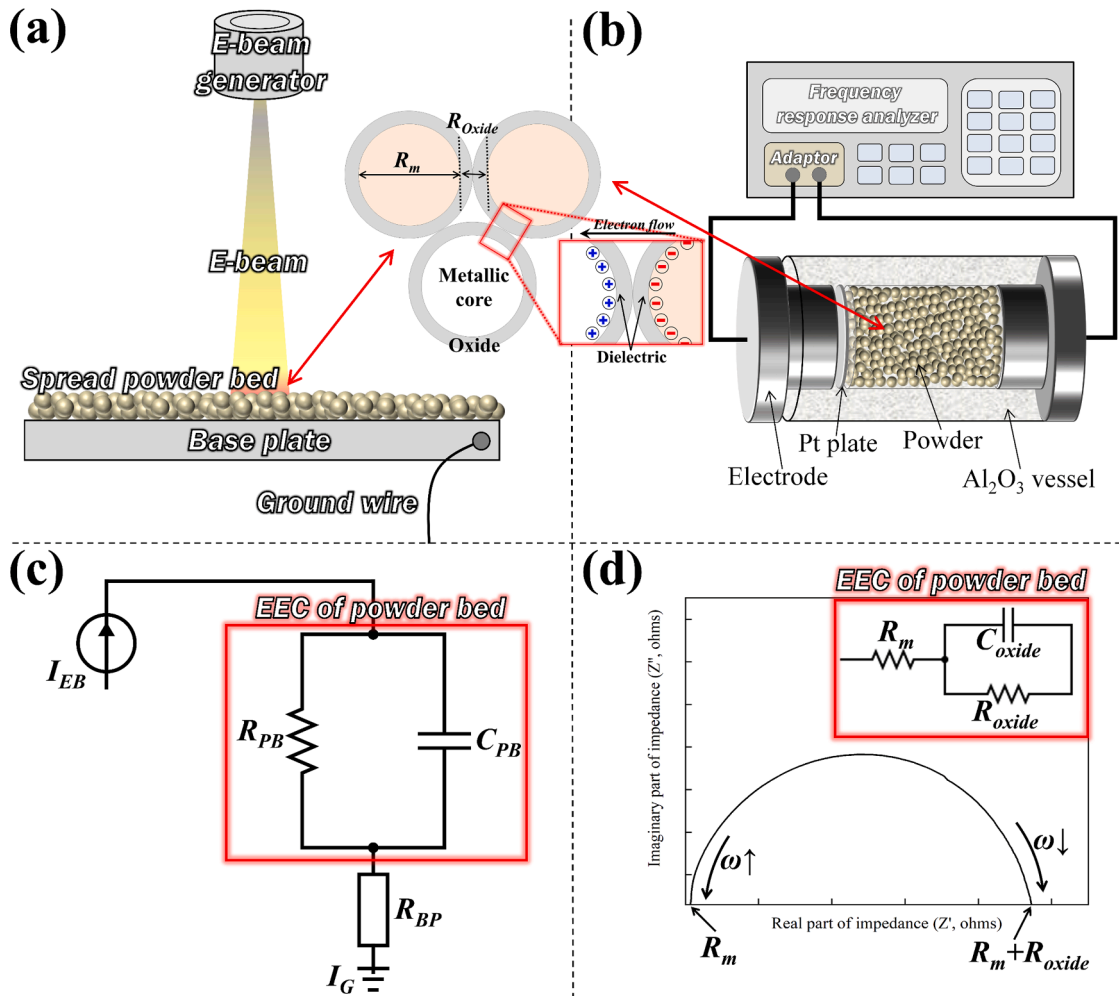


Fig. 6. Schematics of the (a) EB-PBF building process, (b) impedance spectroscopy, (c) electrical equivalent circuit in the EB-PBF building process, and (d) Nyquist plot with the corresponding EEC.

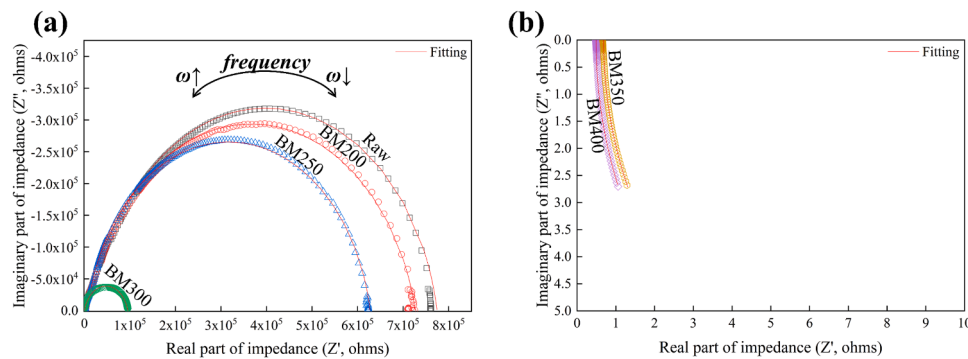


Fig. 7. Nyquist plots of Ti-48Al-2Cr-2Nb powders; (a) gas-atomized, BM200, BM250, BM300, (b) BM350, BM400.

nonequilibrium current distribution due to the surface roughness [20]. The simulated responses (solid red lines) of the EEC model matched well with the experimental data (Fig. 7a and b). The fitting parameters of the EEC model for each specimen are provided in Table 3. In Type 1 of the EEC model,  $R_2$  was higher than  $R_1$  in the raw, BM200, and BM250 powders. The total oxide resistance ( $R_{oxide}$ ) in Type 1 of the EEC model can be expressed as [25].

$$R_{oxide} = R_1 + R_2 \quad (2)$$

The total resistance of the raw powder gradually decreased up to that

of BM250 and thereafter decreased to that of the BM300 powder. Conversely, both  $Q_1$  and  $Q_2$  increased slightly after ball milling, depending on the milling velocities. The minimum  $R_{oxide}$  was obtained in the BM350 and BM400 powders, and they showed an almost similar inductance value ( $L_1$ ). These results suggest that the surface state of the raw powder is significantly changed in the BM300 and BM350 powders after ball milling.

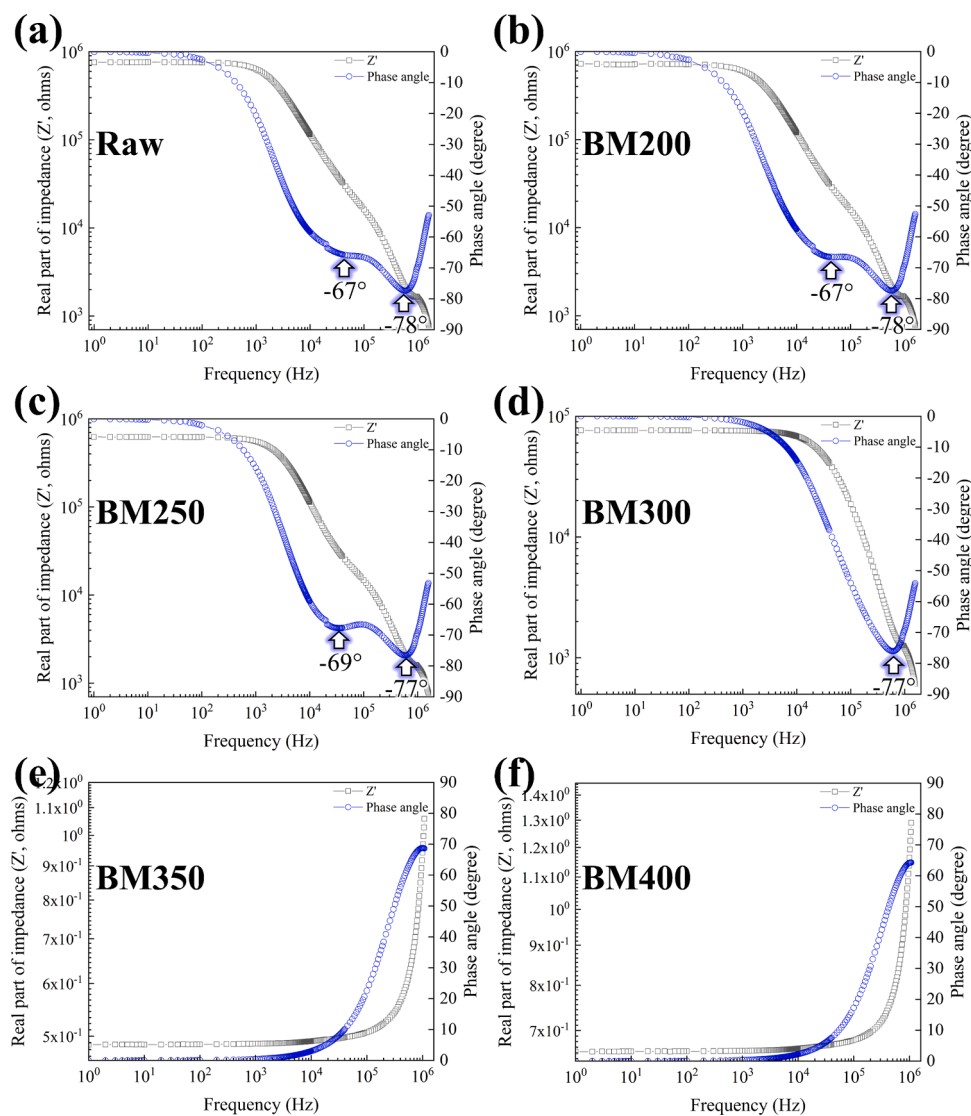


Fig. 8. Bode plot of Ti–48Al–2Cr–2Nb powders; (a) gas-atomized, (b) BM200, (c) BM250, (d) BM300, (e) BM350, and (f) BM400.

### 3.3. XPS and TEM analysis

The XPS spectra of the raw, BM300, and BM350 powders (Fig. 10a) consisted of major alloying elements (Ti 2p, Al 2p, Cr 2p, Nb 3d), carbon (C 1s), and strong oxygen (O 1s) peaks. High-resolution narrow-scan profiles of the Ti 2p, Al 2p, Cr 2p, Nb 3d, and O 1s peaks are shown in Fig. 10b–f. Strong oxide peaks, such as Ti<sup>4+</sup>, Al<sup>3+</sup>, Cr<sup>3+</sup>, and Nb<sup>5+</sup>, were detected in all the samples, indicating that the surfaces of all the powders were insulated by the oxide film. The chemical compositions of the outermost oxide films of the raw and ball-milled powders were determined from the XPS spectra, as shown in Table 4. The outermost oxide of all the powders was mainly composed of Al<sub>2</sub>O<sub>3</sub> and TiO<sub>2</sub>; however, their concentration changed slightly after ball milling. As shown in the Ti 2p spectra (Fig. 10b), the Ti<sup>2+</sup> and Ti<sup>3+</sup> peaks increased in BM300 and BM350, compared with that in the raw powder, and it was approximately 2.1 at% and 2.9 at% in BM350, respectively (Table 4). In the O 1s spectra (Fig. 10f), Al–O and Ti–O peaks were detected, and the concentration of O<sup>2-</sup> gradually decreased in the BM300 and BM350 powders (Table 4). The decrease in O<sup>2-</sup> concentration after ball milling could be due to the formation of Ti<sub>n</sub>O<sub>2n-1</sub> type suboxides, such as TiO and Ti<sub>2</sub>O<sub>3</sub>, on the powder surface. In the Al 2p and Nb 3d spectra, the metallic Al<sup>0</sup> and Nb<sup>0</sup> peaks gradually decreased in the BM300 and BM350 powders after ball milling (Fig. 10c and e). This suggests that the thickness of the

oxide film increased after ball milling due to oxygen contamination.

To investigate both the thickness and composition of the oxide film, the depth profile was performed using Ar<sup>+</sup> ion beam sputtering with an etching rate of 13.6 nm/min, calibrated by the SiO<sub>2</sub> standards. The atomic concentration of each element versus the calculated depth is shown in Fig. 11a, d, and g. It is worth noting here that the O 1s component is always detectable in the XPS survey spectra of the powder even after longer sputtering, owing to their spherical shape [26]. The concentration of the O 1s component gradually decreased, while the Ti 2p and Al 2p components increased with an increasing etching depth. The oxide film thickness can be suspected as half of the maximum O 1s concentration [27], and the calculated thicknesses were 34, 47.6, and 95.2 nm in the raw, BM300, and BM350 powders, respectively. The composition of the oxide film was analyzed using a detailed fitting of the Ti 2p and Al 2p spectra. The concentration of Ti<sup>4+</sup> rapidly decreased, while that of Ti<sup>0</sup> increased with the increasing etching depth. Based on a constant element concentration, the TiO<sub>2</sub> oxide thickness of raw, BM300, and BM350 powders was estimated as 20.4, 27.2, and 20.4 nm, respectively [28]. In the same manner, the thickness of the Al<sub>2</sub>O<sub>3</sub> oxide layer was estimated to be 47.6, 68, and 81.6 nm in the raw, BM300, and BM350 powders, respectively.

The oxide film thickness and composition of the raw and ball-milled powders were further investigated via TEM using a FIBed film from a

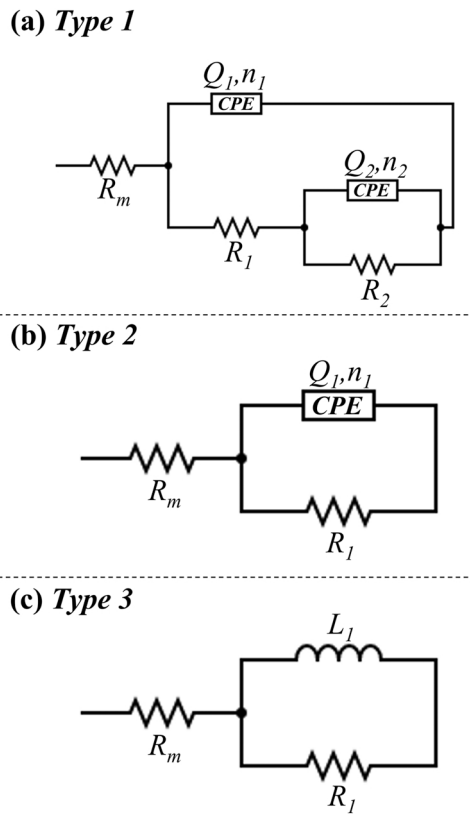


Fig. 9. Three types of electrical equivalent circuit used to fit the impedance data for (a) two time constants, (b) a single time constant, and (c) the resistance and inductance in parallel.

single particle surface. The dark field, element mapping, and line scanning images of the raw, BM300, and BM350 powders are shown in Fig. 12a–c. The oxide film thickness of the raw, BM300, and BM350 powders were measured as 13.4, 46.7, and 91.1 nm, respectively, based on the line scanning results. The increasing trend of oxide film thickness depending on milling velocities is well matched to that of the XPS results, while their thickness difference between the TEM and XPS results could be due to the diameter deviation of the powder particles in the XPS measurement [26]. Furthermore, the maximum oxygen concentration in the line scanning results was approximately 40 at% in the raw powder; however, it was significantly decreased to approximately 16 at% and 20 at% in BM300 and BM350 powders, respectively. (Fig. 12b and c).

### 3.4. Smoking test in the preheating process

To experimentally verify the effect of mechanical ball milling on smoking in the EB-PBF building process, preheating was performed using the raw and ball-milled powders at room temperature. Fig. 13 shows the images of the raw, BM300, and BM350 powders during preheating in the EB-PBF building process. The recorded videos for the smoking test of the powders can be found in appendix 2. The yellow circle indicates the starting point of the electron beam irradiation. In the

raw powder, the powder bed was scattered after preheating for 0.07 s, and it was completely removed into the vacuum chamber after 0.21 s because of charge accumulation. On the other hand, the smoking of BM300 and BM350 was suppressed during the preheating process at room temperature, and those powders can be heated above 800 °C without smoking by manipulating the beam current. These results demonstrate that mechanical ball milling is an effective method for restricting smoking during the EB-PBF building process.

## 4. Discussion

### 4.1. Oxide film of gas-atomized Ti–48Al–2Cr–2Nb powder

The oxide film of the gas-atomized Ti–48Al–2Cr–2Nb powder was investigated via impedance spectroscopy, XPS, and TEM. As shown in Fig. 10b and c, the outermost oxide film of the raw powder mainly consisted of TiO<sub>2</sub> and Al<sub>2</sub>O<sub>3</sub>, and their corresponding depths were estimated to be approximately 20 nm and 48 nm, respectively, based on the depth profile method (Fig. 11b and c). This suggests that the oxide film of the gas-atomized powder consisted of an outer TiO<sub>2</sub> + Al<sub>2</sub>O<sub>3</sub> layer and an inner Al<sub>2</sub>O<sub>3</sub> rich bilayer. Moreover, multiple phase angle peaks representing two types of oxide films were detected in the raw powder (Fig. 8a), and the resistance of the outermost film (R<sub>1</sub>) was much lower than that of the inner film (R<sub>2</sub>), as shown in Table 3. It is well established that the surface oxide film of the Ti-based or TiAl alloy is composed of a bilayer, that is, an inner barrier and outer porous layer; the outer layer showed far lower resistivity than that of the inner layer in the EIS test [22,23]. This indicates that the oxide film structure between the outer and inner films would be different in the gas-atomized Ti–48Al–2Cr–2Nb powder. It has been reported that the formation of the initial oxide film in  $\gamma$ -TiAl alloy is closely related to the oxidation temperature [29]. The formation of TiO<sub>2</sub> is dominant above 1000 °C, while the formation of Al<sub>2</sub>O<sub>3</sub> is favorable below 1000 °C [30–32]. This could be due to the preferential solubility of oxygen atoms to  $\alpha_2$ -Ti<sub>3</sub>Al phase (16 at%) than  $\gamma$ -TiAl phase (2 at%) [30]. Dai et al. [33] reported that the porous oxide films of Ti and Ti alloys are mainly formed at high temperatures due to oxide scale cracking and weak bonding with the metallic core. In the gas atomization process, the liquid metal is atomized by gas jets and thereafter rapidly cooled to room temperature [34]. This indicates that a relatively porous TiO<sub>2</sub> film could form on the outermost surface of Ti–48Al–2Cr–2Nb powder at the initial high temperature, and the oxidation was continued by the fast diffusion of oxygen through the outmost porous TiO<sub>2</sub> layer [35]. Thus, the Al element could be locally enriched underneath the TiO<sub>2</sub> oxide layer, and the relatively dense Al<sub>2</sub>O<sub>3</sub> rich layer was subsequently formed by oxygen diffusion into the metallic core at low temperature. As mentioned earlier, the Al<sub>2</sub>O<sub>3</sub> film was thicker than the TiO<sub>2</sub> film in the gas-atomized Ti–48Al–2Cr–2Nb powder. The Gibbs free energy of the oxidation reaction in Ti and Al elements can be calculated as [36].

$$\Delta G_{TiO_2} = -943490 + 179.08T(298 \sim 1940K). \quad (3)$$

$$\Delta G_{Al_2O_3} = -1120480 + 214.22T(932 \sim 2345K). \quad (4)$$

Thus, the Al<sub>2</sub>O<sub>3</sub> oxide would be more stable than TiO<sub>2</sub> oxide, and its fraction would be further higher in the oxide film of gas-atomized

Table 3

Fitting results from impedance test of raw and ball-milled powders.

Sample	R <sub>m</sub> [Ω]	R <sub>1</sub> [Ω]	Q <sub>1</sub> [nF]	n <sub>1</sub>	R <sub>2</sub> [Ω]	Q <sub>2</sub> [nF]	n <sub>2</sub>	L <sub>1</sub> [μH]
Gas-atomized	0.681	116,842	0.097	0.907	648,431	0.113	0.887	–
BM200	0.697	109,120	0.103	0.896	614,127	0.136	0.871	–
BM250	0.687	80,982	0.111	0.901	544,832	0.134	0.869	–
BM300	0.655	95,171	0.186	0.871	–	–	–	–
BM350	0.661	12.3	–	–	–	–	–	-0.352
BM400	0.495	13.6	–	–	–	–	–	-0.338

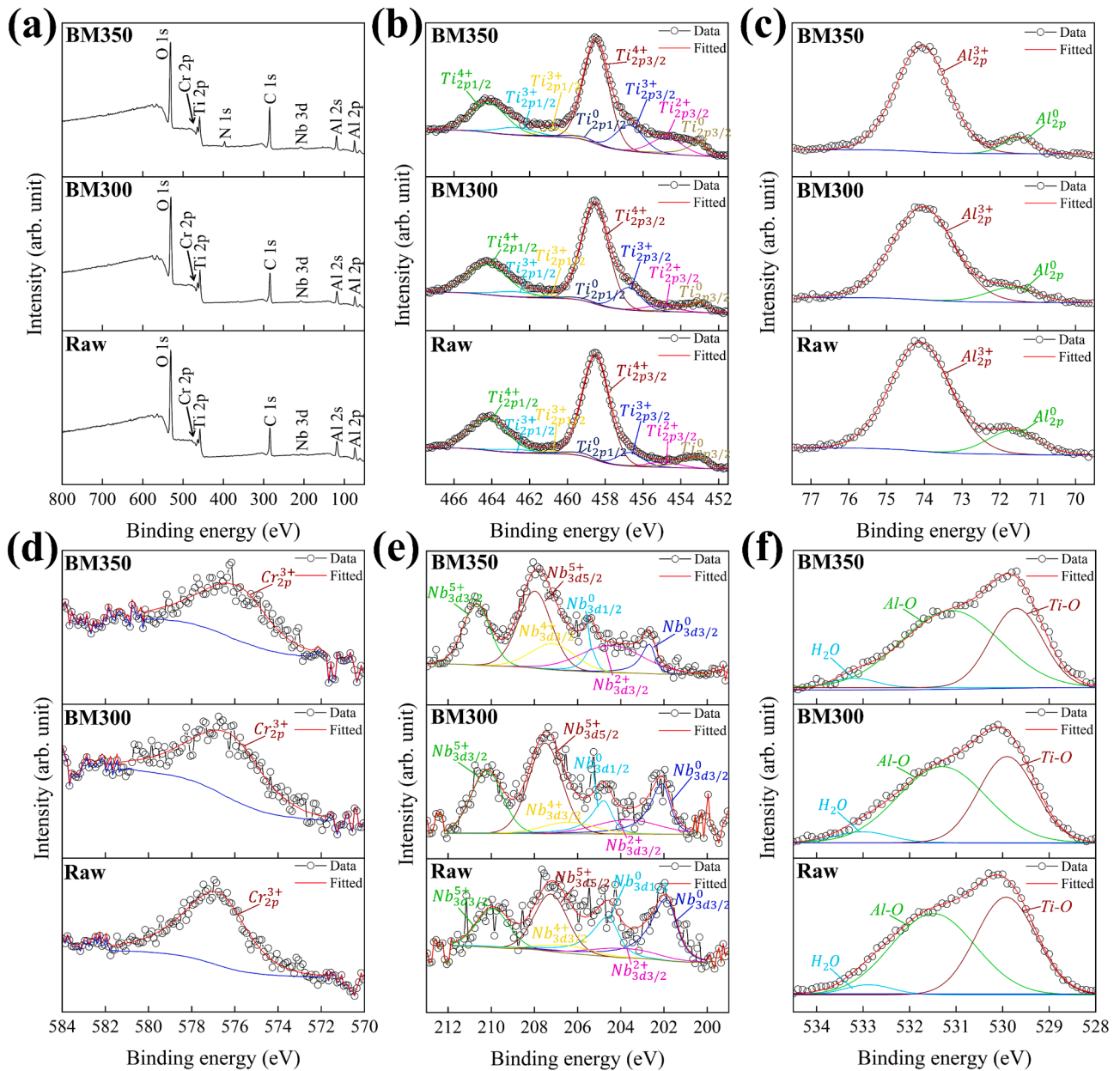


**Fig. 10.** (a) XPS survey spectra on the powder surface and corresponding high-resolution spectra; (b) Ti 2p, (c) Al 2p, (d) Cr 2p, (e) Nb 3d, (f) O 1s in raw, BM300, and BM350 powders.

**Table 4**

Atomic concentration of oxide surface of raw, BM300, and BM350 powders.

Specimen	Atomic concentration of oxide surface (at%)						
	O <sup>2-</sup>	Ti <sup>4+</sup>	Ti <sup>3+</sup>	Ti <sup>2+</sup>	Al <sup>3+</sup>	Cr <sup>3+</sup>	Nb <sup>5+</sup>
Gas-atomized	61.8	8.2	1.1	0.5	26.7	1.6	0.2
BM300	60.1	10.6	1.8	0.6	25.3	1.4	0.3
BM350	57.1	10.6	2.9	2.1	25.6	1.3	0.4

Ti–48Al–2Cr–2Nb powder. In addition, it had been reported that the Nb addition in TiAl alloy can suppress the growth of TiO<sub>2</sub> due to decreased oxygen vacancy concentration by replacing Ti<sup>4+</sup> to Nb<sup>5+</sup> [37]. Therefore, the oxide film of the gas-atomized Ti–48Al–2Cr–2Nb powder could consist of a bilayer with outer porous TiO<sub>2</sub> + Al<sub>2</sub>O<sub>3</sub> and inner dense Al<sub>2</sub>O<sub>3</sub> rich layers.

#### 4.2. Electrical properties of ball-milled powders

In Fig. 2a–d, the deformed surface area expanded with increasing milling velocities, and the entire surface was deformed above 300 rpm. It should be noted that the electrical resistivity of the powder gradually decreased after ball milling, while the thickness of the oxide film increased with the milling velocity. These results indicate that the removal of the oxide film by surface grinding is not a major factor in decreasing the electrical resistivity of the powder. As shown in Fig. 10b, the Ti<sub>n</sub>O<sub>2n-1</sub> type suboxide was observed on the oxide film surface after ball milling, and its quantity gradually increased with the increasing milling velocity (Table 4). Moreover, the oxygen concentration of the oxide film in the raw powder significantly decreased from approximately 40 at% to 20 at% in the BM300 and BM350 powders, owing to the formation of the titanium suboxide phase (Fig. 12a–c). During the ball milling, the surface TiO<sub>2</sub> phase was mechanically deformed by the

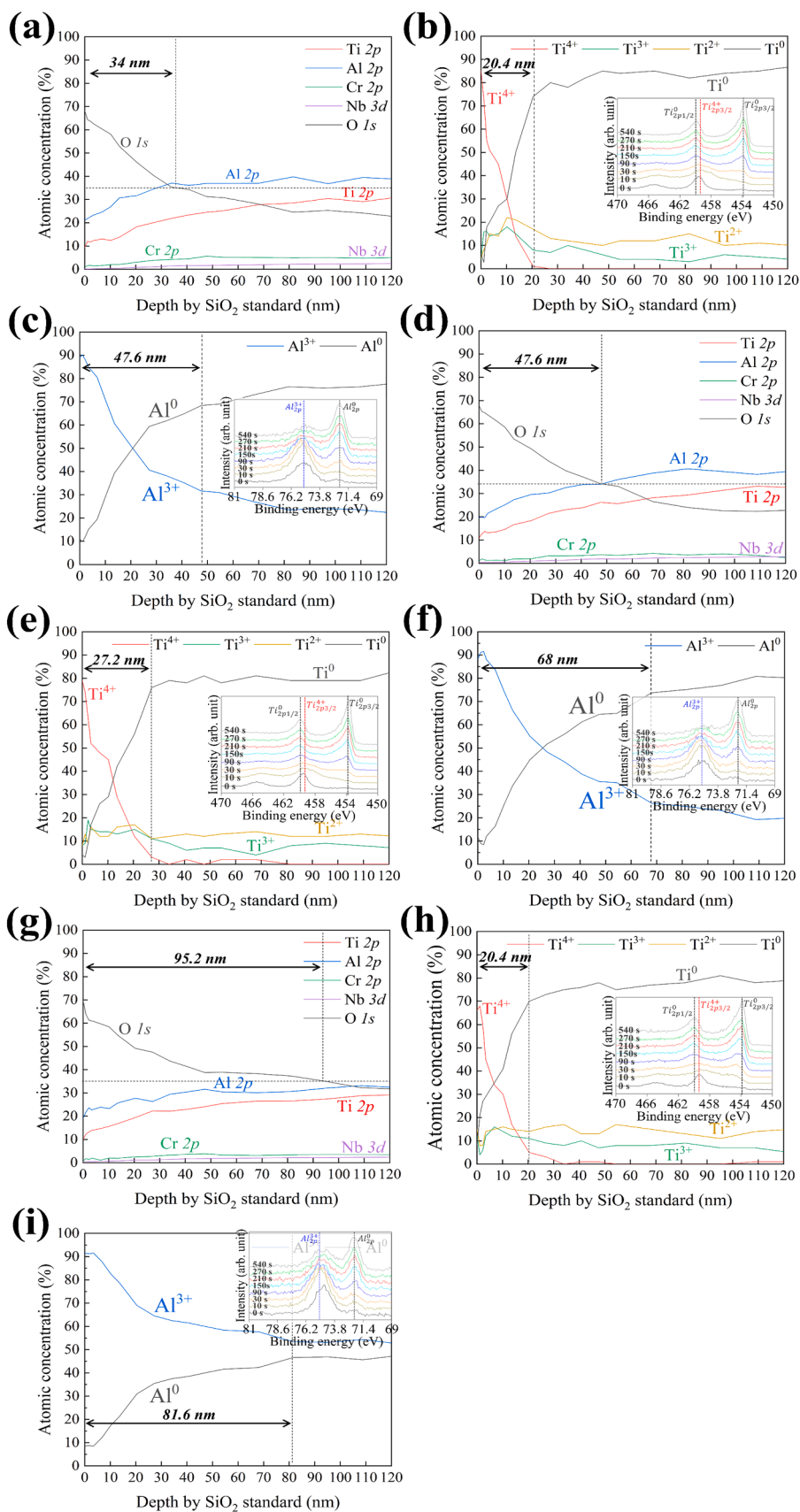


Fig. 11. Depth profile results with the high-resolution spectra of Ti 2p and Al 2p depending on the sputtering time; (a)–(c) raw, (d)–(e) BM300, (g)–(i) BM350 powders.

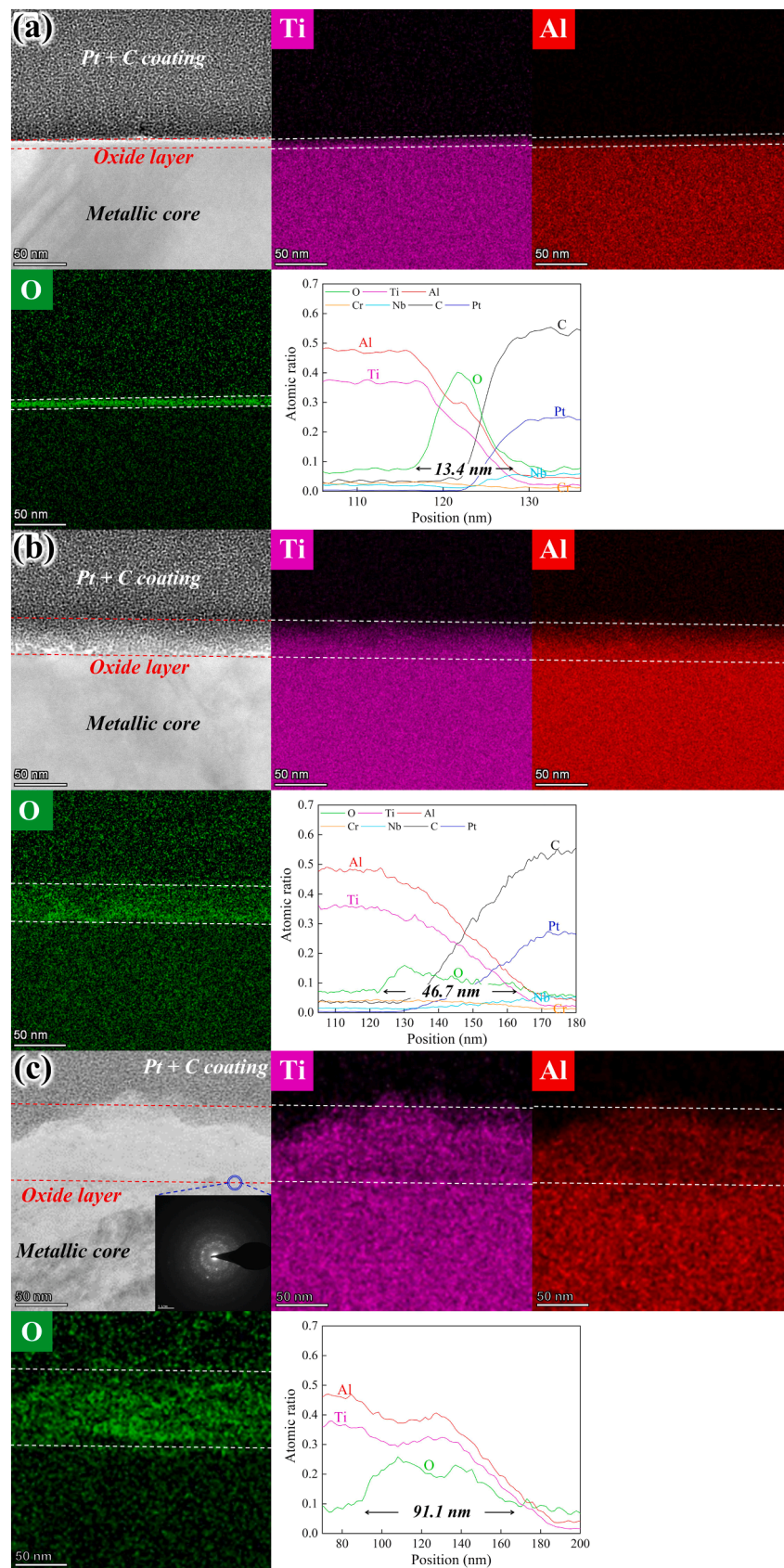


Fig. 12. Dark field TEM image with the elemental mapping and line scanning results; (a) raw, (b) BM300, and (c) BM350 powders.

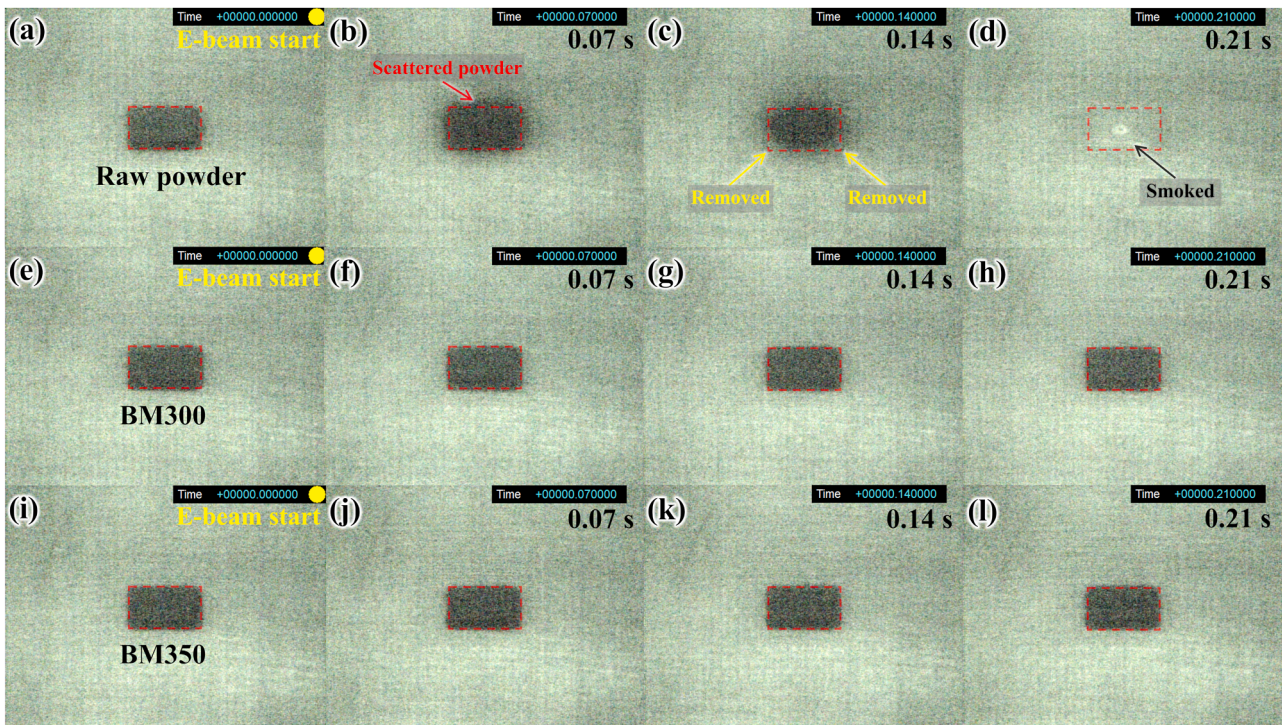


Fig. 13. Snapshot image during preheating in electron beam powder bed fusion manufacturing building process; (a)–(d) raw, (e)–(h) BM300, and (i)–(l) BM350.

WC ball, and the position taken by the  $O^{2-}$  anion in the ordered lattice can be replaced by free electrons to minimize the energetic cost of vacancy formation in the defective crystal. Therefore, the reduction of  $TiO_2$  to  $Ti_nO_{2n-1}$  type suboxide through ball milling can be expressed as [38].



where  $Ti_{Ti}$  and  $O_O$  are the titanium and oxygen atoms on the perfect site of crystal lattice, respectively,  $Ti_{Ti}^*$  is a  $Ti^{3+}$  ion in a titanium site,  $V_O$  is a doubly ionized oxygen vacancy,  $e^-$  is the free electron. These results suggest that the mechanically deformed surface through the ball milling would be replaced with a  $TiO_2 + Al_2O_3 + Ti_nO_{2n-1}$  mixed layer by defect accumulation. Thus, the quantity of  $Ti_nO_{2n-1}$  type suboxides was increased with the milling velocity due to supplied high impact force. It has been reported that the formation of titanium suboxides can significantly alter the electrical conductivity, owing to oxygen vacancies [39, 40]. Xu et al. reported that the electrical resistivity of various  $Ti_nO_{2n-1}$  type suboxides was far lower than that of  $TiO_2$  ( $> 10^{13}$  times) at room temperature [41]. However, the quantity of  $Ti_nO_{2n-1}$  type suboxides was 2.4 at%, and the most of oxide layer consisted of  $TiO_2$  and  $Al_2O_3$  in BM300. Thus, the increased  $Ti_nO_{2n-1}$  type suboxides cannot fully explain why electrical resistance is far decreased after ball milling. Mott [12] suggested the metal-insulator transition arises due to an increase in carrier concentration by doping, causing the formation of degenerate bands. Rajender et al. [42] demonstrated that the band gap narrowing in  $TiO_2$  particles is caused by the combined effect of lattice strain and defects induced by the ball milling. Benson et al. [13] reported that the degenerate doping of titanium dioxide by mechanical strain can result in metal-semiconductor transition due to an increase in carrier concentration. This result suggests that the formation of degenerated  $TiO_2$  by strain accumulation can significantly alter the electrical properties of the surface oxide layer via ball milling. Therefore, the decreased electrical resistance of the ball-milled powder would be due to the combined effect of degenerate doping of the  $TiO_2$  phase by the strain accumulation and formation of  $Ti_nO_{2n-1}$  type suboxides through ball milling.

As shown in Fig. 8a–d, the multiple phase angle peaks at  $-67^\circ$  and  $-78^\circ$  of the raw powder were changed into a single peak at  $-77^\circ$  in the BM300 powder. This result suggests that the outermost  $TiO_2 + Al_2O_3$  film was mechanically deformed and transitioned into the conductive deformed layer containing degenerated  $TiO_2$  and  $Ti_nO_{2n-1}$ -type suboxide through ball milling at 300 rpm. Therefore, the outer conductive deformed layer of BM300 powder did not act as a dielectric, while the undeformed compact inner film sustained its RC circuit. As the milling velocities were further increased above 350 rpm, the resistance in BM350 and BM400 was significantly decreased below  $13.6 \Omega$ , and they showed an inductive behavior that directly proves the high electrical conductivity. This means that the entire insulative oxide film of the raw powder was electrically broken down and replaced with a conductive deformed layer after ball milling at velocities above 350 rpm. Thus, the mechanically deformed oxide layer of BM350 did not act as an insulator; it functioned similar to a conductive metal owing to the increased fraction of degenerated  $TiO_2$  and  $Ti_nO_{2n-1}$  type suboxides. Therefore, it is clearly confirmed that mechanical ball milling is an effective method for increasing the electrical conductivity of Ti–48Al–2Cr–2Nb powder.

#### 4.3. Effect of ball milling on smoking behavior during EB-PBF building process

Powder-bed smoking in the EB-PBF building process is closely related to the electrical interaction among the EEC elements. The interaction force on the powder bed during the preheating process can be expressed as [8].

$$F_{total} = F_{repulsion} + F_{attraction} + F_{electrostatic} \quad (6)$$

The repulsion force ( $F_{repulsion}$ ) between the irradiated electron beam and the negatively charged powder bed can be expressed as follows:

$$F_{repulsion} = \frac{1}{4\pi\epsilon_0} \cdot \frac{Q_{EB} \cdot Q_{PB}}{d_{EB,i}^2} \quad (7)$$

where  $Q_{EB}$  is the negative charge of the electron beam,  $Q_{PB}$  is the

negative charge of the powder bed,  $d_{EB,i}$  is the distance between the beam axis and negatively charged arbitrary particle, and  $\epsilon_0$  is the vacuum permittivity. The attraction force ( $F_{attraction}$ ) between the positively charged base plate and the negatively charged powder bed can be expressed as follows:

$$F_{attraction} = -\frac{1}{4\pi\epsilon_0} \frac{Q_{BP} \cdot Q_{PB}}{d_{BP,i}^2}, \quad (8)$$

where  $Q_{BP}$  is the positive charge of the base plate, and  $d_{BP,i}$  is the distance between the negatively charged arbitrary particle and the positively charged base plate. The electrostatic force ( $F_{electrostatic}$ ) of the negatively charged powder bed can be expressed by

$$F_{electrostatic} = \frac{1}{4\pi\epsilon_0} \sum_{i=1}^{n_p-1} \frac{Q_{PB}^2}{r_i^2}, \quad (9)$$

where  $r_i$  is the radius of the powder-bed particles. Therefore, it is evident that all the driven electrical forces are closely related to the charging degrees of the powder bed. The electrical charging of the powder bed can be expressed as [9].

$$Q_{PB} = J\pi r_i^2 \eta \tau \left( \frac{1 - e^{-\frac{\Delta t}{\tau}}}{1 - e^{-\frac{T}{\tau}}} \right), \quad (10)$$

where  $J$  is the uniform current density of the electron beam,  $\eta$  is the absorption efficiency,  $\tau$  is the relaxation time related to the charging dissipation across the oxide film,  $\Delta t$  is the time for the beam to pass over the powder particle, and period  $T$  is the time required by the beam to raster across the area during preheating. Therefore, the smoking of the powder bed was predominantly affected by the relaxation time between the powder particles. In this study, two types of EEC models were suggested based on impedance spectroscopy, to measure the relaxation time of the powder bed in the EB-PBF building process (Fig. 9a and b). The relaxation time from the EEC model fitting data can be calculated by

$$\tau = R \times C \quad (11)$$

From the CPE model, the true capacitance ( $C$ ) of a single RC circuit can be expressed by [43].

$$C = \frac{(Q \times R)^{1/n}}{R} \quad (12)$$

In the two parallel RC circuits, effective capacitance ( $C_{eff}$ ) can be approximated by [25].

$$C_{eff} = \frac{(Q_1 \times R_m)^{1/m_1}}{R_m} \quad (13)$$

The calculated true capacitance, effective capacitance, and relaxation time are provided in Table 5. The relaxation time of raw powder was significantly decreased approximately 1/16 times from 56.18  $\mu$ s to 3.5  $\mu$ s in BM300, while preserving the particles shape with a small size deviation.

To evaluate the effect of ball milling on smoking during the EB-PBF building process, only the electrostatic force between the two spherical particles that is the dominant electrical force in smoking is considered. The electrostatic force between the two spherical particles can be expressed by [9].

**Table 5**

True capacitance, effective capacitance, and time constant of raw and ball-milled powders.

Sample	C [nF]	C <sub>eff</sub> [nF]	$\tau$ [ $\mu$ s]
Gas-atomized	–	0.0745	56.18
BM200	–	0.0987	54.87
BM250	–	0.1005	52.35
BM300	0.0368	–	3.50

$$F_Q = \frac{Q_p^2}{16\pi\epsilon_0 r_i^2} \cdot f_\xi \quad (14)$$

The normalized force ( $f_\xi$ ) between the contacted spheres encapsulated by the oxide film can be expressed by [44,45].

$$f_\xi = \frac{1}{(\xi + \xi^2) \left( 1 + \frac{1}{2} \log(1 + 1/\xi) \right)^2}, \quad (15)$$

where  $\xi$  is the spacing radius ratio of the oxide film and metallic core ( $r_{oxide}/r_{metal}$ ), as shown in Fig. 14a. The input parameters for the preheating process were used to be  $J = 50.66$  kA/m<sup>2</sup>,  $D_{beam} = 200$   $\mu$ m,  $v = 200$  m/s, and  $\eta = 0.9$  [46], which is same condition to smoke test. The calculated electrostatic force between the two particles gradually decreased after ball milling at velocities up to 250 rpm and significantly decreased to 300 rpm (Fig. 14b). Through mechanical ball milling, the electrostatic force of the raw powder decreased by approximately 1/57 times from  $4.69 \times 10^{-3}$  N to  $8.29 \times 10^{-5}$  N.

As mentioned before, the powder bed smoke of raw powder started after preheating for 0.07 s owing to their long charge dissipation time, and particle scattering was primarily observed in the surface region, as shown in Fig. 13b. When the powder bed is irradiated by the electron beam, the spread particles are electrically negatively charged, while the base plate is positively charged. Therefore, the particles near the base plate are affected by  $F_{attraction}$ , and the smoking of the bottom particles is suppressed. Moreover, the upper site of charged particles could be affected by  $F_{repulsion}$ , while the bottom site of the particles is compressed by the upper deposited particles due to gravitational force; therefore, a significantly higher electrostatic force is required to eliminate the bottom particles into the vacuum chamber compared with that for the surface particles. Therefore, smoking of the powder bed occurs preferentially in the surface area where there is no electrical attraction or compressive force. As the preheating time increased, the outer side of the powder bed was removed. In the preheating process, the scanning pattern of the electron beam was a snake shape, and the returning beam first made contact with the outside of the powder bed. Therefore, electrons accumulate locally on the outside of the powder bed and are first removed into the vacuum chamber because of an induced large amount of electrostatic force. This result indicates that the relaxation time of the raw powder is insufficient for discharging irradiated electrons during the preheating process. However, in the powder bed of BM300, the smoking was suppressed despite the presence of capacitor. This result suggests that the charge accumulation would be relaxed by the formation of the conductive deformed layer, and the electrostatic force between the charged particles would not be enough to occur the particle scattering. Therefore, the smoking of BM300 could be suppressed by rapid charge redistribution owing to the formation of conductive deformed layer. On the other hand, the capacitance response was disappeared, and the inductance response that directly proves metal-like conductivity was observed in BM350. This result indicates that the irradiated electron beam on the powder bed of BM350 could be completely discharged owing to the absence of the capacitor. Therefore, the powder bed smoke of BM350 and BM400 powders could be completely suppressed during the preheating process due to the formation of the resistor-inductor circuit.

The surface modification mechanism of the gas-atomized Ti–48Al–2Cr–2Nb powder via mechanical ball milling is proposed and shown in Fig. 15a–d. The oxide film of the raw powder consisted of outer porous TiO<sub>2</sub> + Al<sub>2</sub>O<sub>3</sub> and dense inner Al<sub>2</sub>O<sub>3</sub> rich double films, and its EEC contained two RC circuits (Fig. 15b). After ball milling at 300 rpm, the outer porous oxide film was mechanically deformed, and it replaced with an electrically conductive deformed layer containing the degenerated TiO<sub>2</sub> and Ti<sub>n</sub>O<sub>2n-1</sub> type suboxide. Therefore, the EEC in BM300 powder consisted of a single RC circuit owing to the preserved dense inner oxide film (Fig. 15c). When the milling velocity is increased

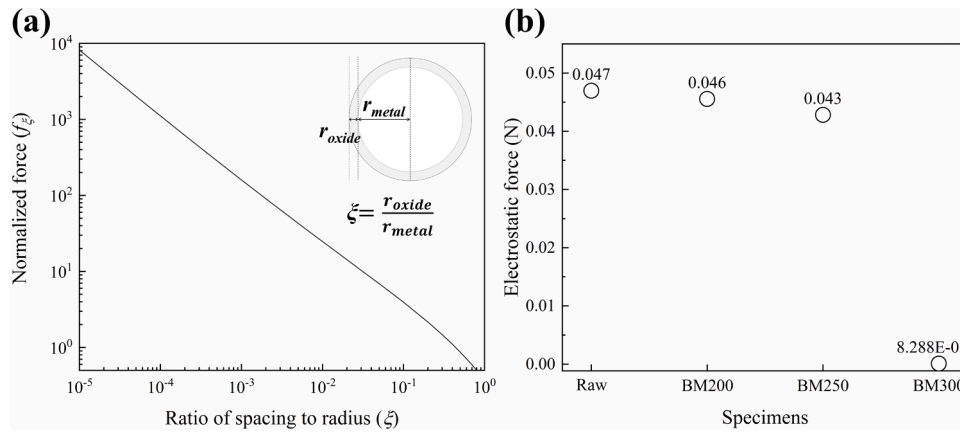


Fig. 14. (a) Normalized force ( $f_z$ ) as a function of radius ratio ( $\xi$ ) and (b) calculated electrostatic force of raw and ball-milled powders.

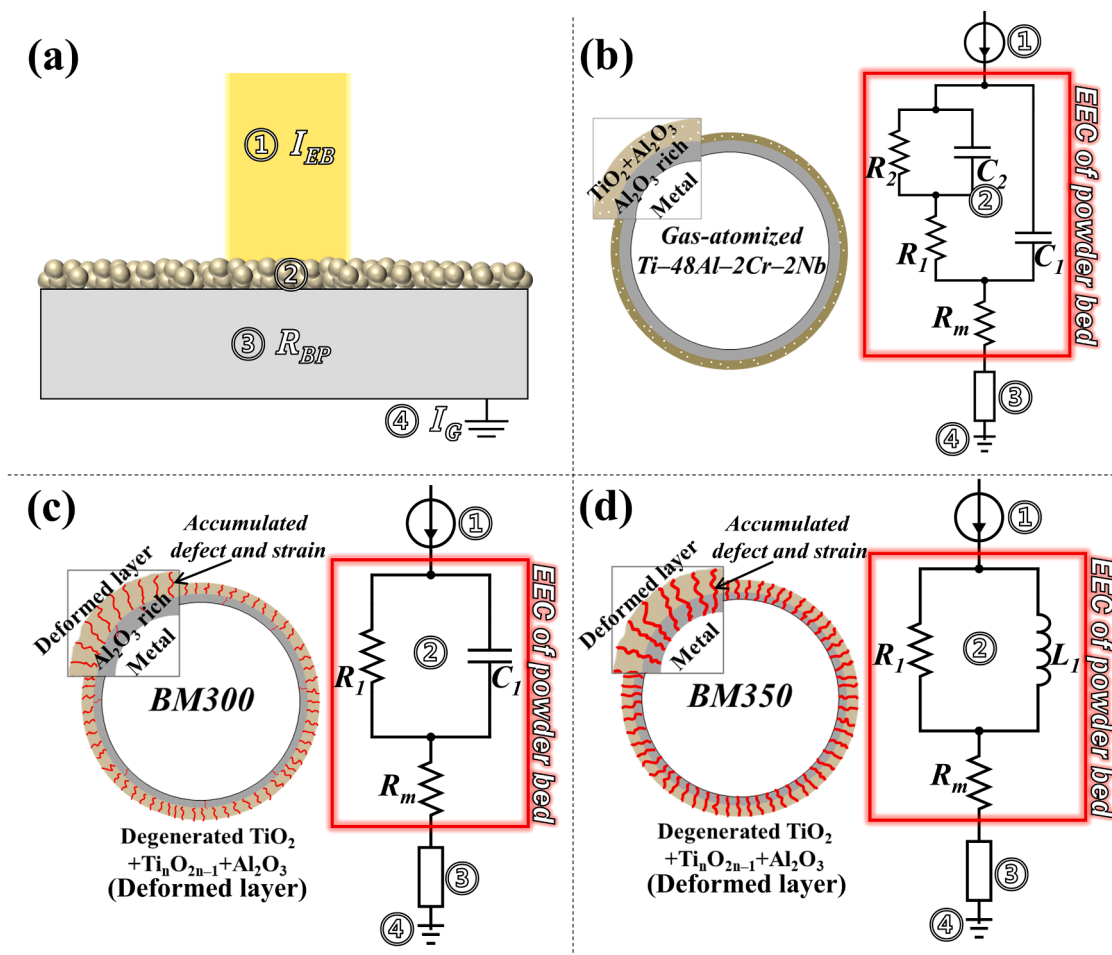


Fig. 15. Schematics of (a) EB-PBF building process, corresponding powder particle and electrical equivalent circuit of Ti-48Al-2Cr-2Nb; (b) raw, (c) BM300, (d) BM350.

to 350 rpm, the entire oxide film is changed into the conductive deformed layer via ball milling, and its EEC consists of a parallel circuit of a resistor-inductor, implying a high electrical conductivity (Fig. 15d). Through mechanical ball milling, smoking of raw powder in the EB-PBF building process can be suppressed, owing to the decreased relaxation time. Therefore, it is believed that mechanical ball milling is a potent method for suppressing smoking in the EB-PBF building process.

Up to now, several studies have suggested a chemical treatment to deoxidize Ti-based powder. The hydride-dehydride (HDH) process is a

well-known method to deoxidize Ti-based alloy utilizing the brittle nature of hydrogenated titanium and the reversible reaction between titanium and hydrogen [47]. However, this process can cause an irregular particle shape that gives rise to many defects in the parts produced via EB-PBF owing to their low flowability [48]. Kim et al. [49,50] reported that Ti-based alloys can be deoxidized by Ca vapor, but this process could change the composition of the alloy system. Furthermore, metal coating and sputtering of the powder is very difficult due to the spherical shape, discrete nature, and high cost [26]. Therefore, the mechanical

ball milling process can be a cost-effective alternative to suppress smoking during the EB-PBF building process and is applicable to various powder feedstocks such as Ti-based, Ni-based alloys without composition change.

## 5. Conclusion

In this study, mechanical ball milling was conducted to evaluate the suppressing effect on powder-bed smoking in the EB-PBF building process, using gas-atomized Ti–48Al–2Cr–2Nb powder at various milling velocities. The oxide film of the gas-atomized Ti–48Al–2Cr–2Nb powder comprised of porous outermost TiO<sub>2</sub> + Al<sub>2</sub>O<sub>3</sub> and dense inner Al<sub>2</sub>O<sub>3</sub> rich bilayers. The oxide film was expanded after ball milling, as the milling velocity increased, owing to oxygen contamination, while the composition of the oxide film was sustained. The EEC of the Ti–48Al–2Cr–2Nb powder was analyzed via impedance spectroscopy. The total resistance of the gas-atomized Ti–48Al–2Cr–2Nb powder gradually decreased after ball milling at a velocity of up to 250 rpm, and the EEC was preserved as two RC circuits. The total resistance of BM300 was significantly decreased due to the formation of the degenerated TiO<sub>2</sub> and Ti<sub>n</sub>O<sub>2n-1</sub>-type suboxide. The EEC of BM300 was composed of a single RC circuit owing to the mechanical deformation of the outer porous oxide film into the conductive deformed layer via ball milling. The relaxation time of the gas-atomized Ti–48Al–2Cr–2Nb powder was decreased from 56.18 μs to 3.50 μs, and the calculated electrostatic force further decreased from  $4.69 \times 10^{-3}$  N to  $8.29 \times 10^{-5}$  N after ball milling under 300 rpm for 30 min. The conductive response was observed after ball milling at a velocity above 350 rpm, owing to the formation of an entire conductive deformed layer, and the EEC was changed to a resistor-inductor circuit. Moreover, it was experimentally validated that smoking in the EB-PBF building process was suppressed in ball-milled powders at 300 and 350 rpm for 30 min. Therefore, the effectiveness of mechanical ball milling to restrict smoking during the EB-PBF building process was demonstrated without the composition change.

## CRedit authorship contribution statement

S. Yim carried out the experiment and simulation, prepared the original draft. H. Bian performed and revised the experiment design and discussed the simulation, revised the manuscript. K. Aoyagi and K. Yamanaka discussed the result and revised the manuscript. A. Chiba as the supervision and program leader performed the experiment design and discussion, provided the funding. K. Yanagihara, S. Kitamura, H. Manabe, and Yohei Daino performed the smoke test experiment. Y. Hayasaka performed STEM observation. All authors discussed the results.

## Declaration of Competing Interest

The authors declare the following financial interests/personal relationships which may be considered as potential competing interests: One of the authors of this article are a part of the Editorial Board of the journal. To avoid a potential conflict of interest, the re-sponsibility for the editorial and peer-review process of this article was handled by a different editor. Furthermore, the authors of this article were removed from the peer review process and had no, and will not have, any access to confidential information related to the editorial process of this article.

## Acknowledgments

This work was partially supported by JSPS KAKENHI [grant number 18H03834 and 21k14432]. This research was also supported by "Materials Integration for Revolutionary Design System of structure Materials" of the Cross-Ministerial Strategic Innovation Promotion Program (SIP) of Japan Science and Technology Agency (JST). This work was also

based on results obtained from a project commissioned by the New Energy and Industrial Technology Development Organization (NEDO) [JPNP14014]. This work was partly supported by the Technology Research Association for Future Additive Manufacturing (TRAFAM). This work is also based on the results obtained from a project [JPNP19007], commissioned by the New Energy and Industrial Technology Development Organization (NEDO).

## Appendix A. Supporting information

Supplementary data associated with this article can be found in the online version at doi:10.1016/j.addma.2022.102634.

## References

- [1] H. Clemens, H. Kestler, Processing and applications of intermetallic  $\gamma$ -TiAl-based alloys, *Adv. Eng. Mater.* 2 (2000) 551–570, [https://doi.org/10.1002/1527-2648\(200009\)2:9<551::AID-ADEM551>3.0.CO;2-U](https://doi.org/10.1002/1527-2648(200009)2:9<551::AID-ADEM551>3.0.CO;2-U).
- [2] S.Z. Zhang, C.J. Zhang, Z.X. Du, Z.P. Hou, P. Lin, Y.Y. Chen, Microstructure and tensile properties of hot forged high Nb containing TiAl based alloy with initial near lamellar microstructure, *Mater. Sci. Eng. A.* 642 (2015) 16–21, <https://doi.org/10.1016/j.msea.2015.06.066>.
- [3] C. Körner, Additive manufacturing of metallic components by selective electron beam melting - a review, *Int. Mater. Rev.* 61 (2016) 361–377, <https://doi.org/10.1080/09506608.2016.1176289>.
- [4] L.E. Murr, S.M. Gaytan, A. Ceylan, E. Martinez, J.L. Martinez, D.H. Hernandez, B. I. Machado, A.A. Ramirez, F. Medina, S. Collins, R.B. Wicker, Characterization of titanium aluminide alloy components fabricated by additive manufacturing using electron beam melting, *Acta Mater.* 58 (2010) 1887–1894, <https://doi.org/10.1016/j.actamat.2009.11.032>.
- [5] S. Biamino, A. Penna, U. Ackelid, S. Sabbadini, O. Tassa, P. Fino, M. Pavese, P. Gennaro, C. Badini, Electron beam melting of Ti-48Al-2Cr-2Nb alloy: microstructure and mechanical properties investigation, *Intermetallics* 19 (2011) 776–781, <https://doi.org/10.1016/j.intermet.2010.11.017>.
- [6] W. Kan, B. Chen, C. Jin, H. Peng, J. Lin, Microstructure and mechanical properties of a high Nb-TiAl alloy fabricated by electron beam melting, *Mater. Des.* 160 (2018) 611–623, <https://doi.org/10.1016/j.matdes.2018.09.044>.
- [7] M. Sigl, S. Lutzmann, M.F. Zaeh, Transient physical effects in electron beam sintering, *17th Solid Free. Fabr. Symp. SFF* 2006. 2006, 464–477.
- [8] C. Eschey, S. Lutzmann, M.F. Zaeh, Examination of the powder spreading effect in Electron Beam Melting (EBM), *20th Annu. Int. Solid Free. Fabr. Symp. SFF* (2009) 308–319.
- [9] Z.C. Cordero, H.M. Meyer, P. Nandwana, R.R. Dehoff, Powder bed charging during electron-beam additive manufacturing, *Acta Mater.* J. 124 (2017) 437–445, <https://doi.org/10.1016/j.actamat.2016.11.012>.
- [10] A. Chiba, Y. Daino, K. Aoyagi, K. Yamanaka, Smoke suppression in electron beam melting of inconel 718 alloy powder based on insulator–metal transition of surface, *Materials* 14 (2021), <https://doi.org/10.3390/ma14164662>.
- [11] M. Kahnert, S. Lutzmann, M.F. Zaeh, Layer formations in electron beam sintering, *18th Solid Free. Fabr. Symp. SFF* 2007. 2007, 88–99.
- [12] N.F. Mott, The basis of the electron theory of metals, with special reference to the transition metals, *Proc. Phys. Soc. Sect. A.* 62, 1949 416–422. doi:10.1088/0370-1298/62/7/303.
- [13] E.E. Benson, E.M. Miller, S.U. Nanayakkara, D. Svedruzic, S. Ferrere, N.R. Neale, J. Van de Lagemaat, B.A. Gregg, Semiconductor-to-metal transition in rutile TiO<sub>2</sub> induced by tensile strain, *Chem. Mater.* 29 (2017) 2173–2179, <https://doi.org/10.1021/acs.chemmater.6b04881>.
- [14] G. Greczynski, L. Hultman, X-ray photoelectron spectroscopy: towards reliable binding energy referencing, *Prog. Mater. Sci.* 107 (2020) 100591–100636, <https://doi.org/10.1016/j.pmatsci.2019.100591>.
- [15] B. Liu, M. Wang, Y. Du, J. Li, Size-dependent structural properties of a high-Nb TiAl alloy powder, *Materials* 13 (2020) 1–7, <https://doi.org/10.3390/ma13010161>.
- [16] X. Lu, Q. Li, M. Guo, J. Zhu, K. Yang, Y. Shu, J. He, Study of the agglomeration behaviour of surface-modified molybdenum powder, *Met. Mater. Int* 17 (2020), <https://doi.org/10.1007/s12540-020-00651-7>.
- [17] J. Guyon, A. Hazotte, E. Bouzy, Evolution of metastable a phase during heating of Ti48Al2Cr2Nb intermetallic alloy, *J. Alloy. Compd.* 656 (2016) 667–675, <https://doi.org/10.1016/j.jallcom.2015.09.179>.
- [18] J.G. Ramirez, R. Schmidt, A. Sharoni, M.E. Gómez, I.K. Schuller, E.J. Patiño, Ultra-thin filaments revealed by the dielectric response across the metal-insulator transition in VO<sub>2</sub>, *Appl. Phys. Lett.* 102 (2013) 2011–2015, <https://doi.org/10.1063/1.4792052>.
- [19] K.V. Korshunov, M.V. Tsarev, V.V. Mokrushin, A.M. Shapovalov, E.V. Zabavin, Application of impedance spectroscopy to study oxidized powders of titanium hydride, *J. Alloy. Compd.* 645 (2015) 140–143, <https://doi.org/10.1016/j.jallcom.2015.01.131>.
- [20] E. von Hauf, Impedance spectroscopy for emerging photovoltaics, *J. Phys. Chem. C* 123 (2019) 11329–11346, <https://doi.org/10.1021/acs.jpcc.9b00892>.
- [21] H.H. Ge, G.D. Zhou, W.Q. Wu, Passivation model of 316 stainless steel in simulated cooling water and the effect of sulfide on the passive film, *Appl. Surf. Sci.* 211 (2003) 321–334, [https://doi.org/10.1016/S0169-4332\(03\)00355-6](https://doi.org/10.1016/S0169-4332(03)00355-6).

- [22] L.L. Rodriguez, P.A. Sundaram, Corrosion behavior of plasma electrolytically oxidized gamma titanium aluminide alloy in simulated body fluid, *Mater. Chem. Phys.* 181 (2016) 67–77, <https://doi.org/10.1016/j.matchemphys.2016.06.034>.
- [23] Y. Wang, Z. Xu, A. Zhang, Anodic characteristics and electrochemical machining of two typical g-TiAl alloys and its quantitative dissolution model in NaNO<sub>3</sub> solution, *Electrochim. Acta* 331 (2020) 135429–135441, <https://doi.org/10.1016/j.electacta.2019.135429>.
- [24] M.V. Tsarev, V.V. Mokrushin, K.V. Korshunov, A.M. Shapovalov, A.Y. Postnikov, I. A. Tsareva, O.Y. Zbrodina, D.G. Ivanova, E.V. Zabavin, A.E. Kanunov, Preparation of green mixtures for SHS reactions: characterization by impedance spectroscopy, *Int. J. Self Propagating High. Temp. Synth.* 29 (2020) 22–25, <https://doi.org/10.3103/S1061386220010136>.
- [25] K. Yamanaka, H. Shiratori, M. Mori, K. Omura, T. Fujieda, K. Kuwabara, A. Chiba, Corrosion mechanism of an equimolar AlCoCrFeNi high-entropy alloy additively manufactured by electron beam melting, *Npj Mater. Degrad.* 4 (2020) 1–12, <https://doi.org/10.1038/s41529-020-00127-4>.
- [26] Y.H. Zhou, S.F. Lin, Y.H. Hou, D.W. Wang, P. Zhou, P.L. Han, Y.L. Li, M. Yan, Layered surface structure of gas-atomized high Nb-containing TiAl powder and its impact on laser energy absorption for selective laser melting, *Appl. Surf. Sci.* 441 (2018) 210–217, <https://doi.org/10.1016/j.apsusc.2018.01.296>.
- [27] L. Zhang, Y. Duan, R. Gao, J. Yang, K. Wei, D. Tang, T. Fu, The effect of potential on surface characteristic and corrosion resistance of anodic oxide film formed on commercial pure titanium at the potentiodynamic-aging mode ling, *Materials* 12 (2019) 1–18, <https://doi.org/10.3390/ma12030370>.
- [28] D. Chasoglou, E. Hryha, M. Norell, L. Nyborg, Characterization of surface oxides on water-atomized steel powder by XPS/AES depth profiling and nano-scale lateral surface analysis, *Appl. Surf. Sci.* 268 (2013) 496–506, <https://doi.org/10.1016/j.apsusc.2012.12.155>.
- [29] J. Geng, G. Gantner, P. Oelhafen, P.K. Datta, Initial oxidation of Ti-Al intermetallics: an in situ MXPS study, *Appl. Surf. Sci.* 158 (2000) 64–74, [https://doi.org/10.1016/S0169-4332\(99\)00583-8](https://doi.org/10.1016/S0169-4332(99)00583-8).
- [30] V. Maurice, G. Despert, S. Zanna, P. Josso, M.-P. Bacos, P. Marcus, XPS study of the initial stages of oxidation of a2-Ti3Al and c-TiAl intermetallic alloys, *Acta Mater.* 55 (2007) 3315–3325, <https://doi.org/10.1016/j.actamat.2007.01.030>.
- [31] H.L. Du, A. Aljarany, P.K. Datta, J.S. Burnell-Gray, Oxidation behaviour of Ti-46.7Al-1.9W-0.5Si in air and Ar-20%O<sub>2</sub> between 750 and 950°C, *Corros. Sci.* 47 (2005) 1706–1723, <https://doi.org/10.1016/j.corsci.2004.08.014>.
- [32] G.H. Meier, F.S. Pettit, The oxidation behavior of intermetallic compounds, *Mater. Sci. Eng. A* 153 (1992) 548–560, [https://doi.org/10.1016/0921-5093\(92\)90250-5](https://doi.org/10.1016/0921-5093(92)90250-5).
- [33] J. Dai, J. Zhu, C. Chen, F. Weng, High temperature oxidation behavior and research status of modifications on improving high temperature oxidation resistance of titanium alloys and titanium aluminides: a review, *J. Alloy. Compd.* 685 (2016) 784–798, <https://doi.org/10.1016/j.jallcom.2016.06.212>.
- [34] X. Li, Q. Zhu, S. Shu, J. Fan, S. Zhang, Fine spherical powder production during gas atomization of pressurized melts through melt nozzles with a small inner diameter, *Powder Technol.* 356 (2019) 759–768, <https://doi.org/10.1016/j.powtec.2019.09.023>.
- [35] F.P. Ping, Q.M. Hu, A.V. Bakulin, S.E. Kulkova, R. Yang, Alloying effects on properties of Al<sub>2</sub>O<sub>3</sub> and TiO<sub>2</sub> in connection with oxidation resistance of TiAl, *Intermetallics* 68 (2016) 57–62, <https://doi.org/10.1016/j.intermet.2015.09.005>.
- [36] S. Tian, H. Jiang, G. Zhang, Y. Zhang, H. Lin, Y. Yang, Investigation on the initial oxidation behavior of TiAl alloy, *Mater. Res. Express* 6 (2019), 106595, <https://doi.org/10.1088/2053-1591/ab3ce6>.
- [37] H. Jiang, M. Hirohata, Y. Lu, H. Imanari, Effect of Nb on the high temperature oxidation of Ti-(0-50at%)Al, *Scr. Mater.* 46 (2002) 639–643, [https://doi.org/10.1016/S1359-6462\(02\)00042-8](https://doi.org/10.1016/S1359-6462(02)00042-8).
- [38] R. Amade, P. Heitjans, S. Indris, M. Finger, A. Haeger, D. Hesse, Defect formation during high-energy ball milling in TiO<sub>2</sub> and its relation to the photocatalytic activity, *J. Photochem. Photobiol. A Chem.* 207 (2009) 231–235, <https://doi.org/10.1016/j.jphotochem.2009.07.015>.
- [39] S. Nandi, R. Tripathi, G. Das Adhikary, P. Kumar, A. Misra, Ultrahigh infrared photoresponse in titanium sesquioxide at mott-insulator transition, *Adv. Mater. Interfaces* 7 (2020) 1–7, <https://doi.org/10.1002/admi.202001091>.
- [40] I.H. Hwang, B. Jiang, Z. Jin, C.I. Park, S.W. Han, Anomalous structural disorder and distortion in metal-to-insulator-transition Ti<sub>2</sub>O<sub>3</sub>, *J. Appl. Phys.* 119 (2016), 014905, <https://doi.org/10.1063/1.4939290>.
- [41] X. Baoqiang, H.Y. Sohn, Y.M. A. Y. Lan, Structures, preparation and applications of titanium suboxides, *RSC Adv.* 9 (2016) 79706–79722, <https://doi.org/10.1039/c6ra14507h>.
- [42] G. Rajender, P.K. Giri, Strain induced phase formation, microstructural evolution and bandgap narrowing in strained TiO<sub>2</sub> nanocrystals grown by ball milling, *J. Alloy. Compd.* 676 (2016) 591–600, <https://doi.org/10.1016/j.jallcom.2016.03.154>.
- [43] B. Hirschorn, M.E. Orazema, B. Tribollet, V. Vivier, I. Frateur, M. Musiani, Determination of effective capacitance and film thickness from constant-phase-element parameters, *Electrochim. Acta* 55 (2010) 6218–6227, <https://doi.org/10.1016/j.electacta.2009.10.065>.
- [44] J. Crowley, Simple Expressions for Force and Capacitance for a Conductive Sphere near a Conductive Wall, *Proc. Electrochem. Soc. Am. Annu. Meet. Electrochem. Soc.* (2008) 1–15.
- [45] S. Banerjee, M. Levy, Approximate Capacitance Expressions for Two Equal Sized Conducting Spheres, *Proc. Electrochem. Soc. Am. Annu. Meet. Electrochem. Soc.* (2014).
- [46] Y. Zhao, Y. Koizumi, K. Aoyagi, D. Wei, K. Yamanaka, A. Chiba, Molten pool behavior and effect of fluid flow on solidification conditions in selective electron beam melting (SEBM) of a biomedical Co-Cr-Mo alloy, *Addit. Manuf.* 26 (2019) 202–214, <https://doi.org/10.1016/j.addma.2018.12.002>.
- [47] J.M. Oh, K.M. Roh, B.K. Lee, C.Y. Suh, W. Kim, H. Kwon, J.W. Lim, Preparation of low oxygen content alloy powder from Ti binary alloy scrap by hydrogenation-dehydrogenation and deoxidation process, *J. Alloy. Compd.* 593 (2014) 61–66, <https://doi.org/10.1016/j.jallcom.2014.01.033>.
- [48] S.P. Narra, Z. Wu, R. Patel, J. Capone, M. Paliwal, J. Beuth, A. Rollett, Use of non-spherical hydride-dehydride (HDH) powder in powder bed fusion, *Addit. Manuf.* 34 (2020), 101188, <https://doi.org/10.1016/j.addma.2020.101188>.
- [49] T. Kim, J.M. Oh, G.H. Cho, H. Chang, H.D. Jang, J.W. Lim, Surface and internal deoxidation behavior of titanium alloy powder deoxidized by Ca vapor: comparison of the deoxidation capability of solid solution and intermetallic titanium alloys, *Appl. Surf. Sci.* 534 (2020), 147623, <https://doi.org/10.1016/j.apsusc.2020.147623>.
- [50] T.H. Okabe, T. Oishi, K. Ono, Deoxidation of titanium aluminide by Ca-Al alloy under controlled aluminum activity, *Metall. Trans. B* 23 (1992) 583–590, <https://doi.org/10.1007/BF02649718>.